7714 *Inorg. Chem.* **2009**, *48*, 7714–7728
DOI: 10.1021/ic900651n

Inorganic Chemistry
Article

On the Reactivity of $F_3S{\equiv}NXeF^+$: Syntheses and Structural Characterizations of $[F_4S{=}N{-}Xe{\cdots}N{\equiv}SF_3][AsF_6]$, a Rare Example of a N−Xe−N Linkage, and $[F_3S(N{\equiv}SF_3)_2][AsF_6]$

Gregory L. Smith and Gary J. Schrobilgen*

Department of Chemistry, McMaster University, Hamilton, Ontario L8S 4M1, Canada

Received April 2, 2009

The $F_4S{=}N{-}Xe{\cdots}N{\equiv}SF_3^+$ cation has been synthesized as the AsF_6^- salt by rearrangement of $[F_3S{\equiv}NXeF][AsF_6]$ in $N{\equiv}SF_3$ solvent at 0 °C. Deep yellow $[F_4S{=}N{-}Xe{\cdots}N{\equiv}SF_3][AsF_6]$, which crystallized from a $N{\equiv}SF_3$ solution at −10 °C, was characterized by Raman spectroscopy (−160 °C) and by single-crystal X-ray diffraction (−173 °C). The Xe−N bond length (2.079(3) Å) of the $F_4S{=}N{-}Xe{\cdots}N{\equiv}SF_3^+$ cation is among the shortest Xe−N bonds presently known. The $F_4S{=}NXe^+$ cation interacts with $N{\equiv}SF_3$ by means of a Xe···N donor-acceptor bond (2.583(3) Å) that is significantly longer than the primary Xe−N bond (2.079(3)Å) but significantly shorter than the sum of the Xe and N van der Waals radii (3.71 Å). The $F_4S{=}N{-}Xe{\cdots}N{\equiv}SF_3^+$ cation undergoes a redox decomposition in $N{\equiv}SF_3$ at 0 °C, forming $[F_3S(N{\equiv}SF_3)_2][AsF_6]$, *cis*-$N_2F_2$, and Xe, which were characterized by low-temperature Raman spectroscopy in the solid state and by ^{19}F NMR spectroscopy in $N{\equiv}SF_3$ solvent (0 °C). Colorless $[F_3S(N{\equiv}SF_3)_2][AsF_6]$ crystallized from $N{\equiv}SF_3$ at −10 °C and was characterized by low-temperature, single-crystal X-ray diffraction. The S(IV) atom of $F_3S(N{\equiv}SF_3)_2^+$ has long contacts with the N atoms of two $N{\equiv}SF_3$ molecules and a F ligand of a neighboring AsF_6^- anion. The arrangement of long contacts avoids, to the maximum extent, the F atoms of SF_3^+ and the nonbonding electron pair situated on the pseudo-3-fold axis opposite the F ligands of SF_3^+, providing distorted octahedral coordination about the S(IV) atom. Quantum-chemical calculations using MP2, B3LYP, and PBE1PBE methods were employed to arrive at the gas-phase geometries, charges, bond orders, valencies, and vibrational frequencies for $F_4S{=}N{-}Xe{\cdots}N{\equiv}SF_3^+$ and $F_3S(N{\equiv}SF_3)_2^+$ to aid in the assignments of experimental vibrational frequencies. The $F_4S{=}N{-}Xe{\cdots}N{\equiv}SF_3^+$ cation expands the known chemistry of the $F_4S{=}N{-}$ group and is the first example of a N−Xe−N linkage to be structurally characterized by single-crystal X-ray diffraction.

Introduction

Until recently, the only xenon-nitrogen bonded species having formally sp^2-hybridized nitrogen bonded to xenon were the XeF^+ adducts of *s*-trifluorotriazine[1] and several perfluoropyridines;[2] the μ-imidobis(sulfurylfluoride) ($-N(SO_2F)_2$) derivatives of xenon(II), $FXeN(SO_2F)_2$,[3−5] $Xe[N(SO_2F)_2]_2$,[4,6] $F[XeN(SO_2F)_2]_2^+$,[4,6,7] and $XeN(SO_2F)_2^+$;[7] and the related trifluoromethyl derivative $Xe[N(SO_2CF_3)_2]_2$.[8] The pentacoordinated sulfur(VI) cations, $F_4S{-}N(CH_3)_2^+$,[9] $F_4S{-}N(CH_2CH_3)_2^+$,[10] and $F_4S{-}NC_5H_{10}^+$,[10] have been structurally characterized by ^{19}F NMR spectroscopy, which showed that rotation about their S−N bonds was rapid on the NMR time scale. Most recently, the $F_4S{=}NXe^+$ and $F_4S{=}NH_2^+$ cations[11] were reported from this laboratory and represent the only known cationic derivatives of the $F_4S{=}N{-}$ group and the first sp^2-hybridized imido species in which the nitrogen bonded to xenon is doubly bonded to sulfur. Neither $F_4S{=}NXe^+$ nor $F_4S{=}NH_2^+$ exhibited rotation about their S=N bonds on the NMR time scale.

The basicity of thiazyl trifluoride, $N{\equiv}SF_3$, has been demonstrated by its reactions with BF_3, AsF_5, and SbF_5 in

*To whom correspondence should be addressed. E-mail: schrobil@mcmaster.ca.

(1) Schrobilgen, G. J. *J. Chem. Soc., Chem. Commun.* **1988**, 1506–1508.
(2) Emara, A. A. A.; Schrobilgen, G. J. *J. Chem. Soc., Chem. Commun.* **1988**, 257–259.
(3) LeBlond, R. D.; DesMarteau, D. D. *J. Chem. Soc., Chem. Commun.* **1974**, 555–556.
(4) DesMarteau, D. D.; LeBlond, R. D.; Hossain, S. F.; Nothe, D. *J. Am. Chem. Soc.* **1981**, *103*, 7734–7739.
(5) Sawyer, J. F.; Schrobilgen, G. J.; Sutherland, S. J. *Inorg. Chem.* **1982**, *21*, 4064–4072.
(6) Schumacher, G. A.; Schrobilgen, G. J. *Inorg. Chem.* **1983**, *22*, 2178–2183.
(7) Faggiani, R.; Kennepohl, D. K.; Lock, C. J. L.; Schrobilgen, G. J. *Inorg. Chem.* **1986**, *25*, 563–571.
(8) Foropoulos, J. J.; DesMarteau, D. D. *J. Am. Chem. Soc.* **1982**, *104*, 4260–4261.
(9) Meier, T.; Mews, R. *Angew. Chem., Int. Ed. Engl.* **1985**, *24*, 344–345.
(10) Meier, T.; Mews, R. *J. Fluorine Chem.* **1994**, *66*, 141–146.
(11) Smith, G. L.; Mercier, H. P. A.; Schrobilgen, G. J. *J. Am. Chem. Soc.* **2009**, *131*, 7272–7286.

Published on Web 07/21/2009

Scheme 1. Proposed Mechanism for the $N{\equiv}SF_3$-Promoted Fluoride Rearrangement of $F_3S{\equiv}NXeF^+$

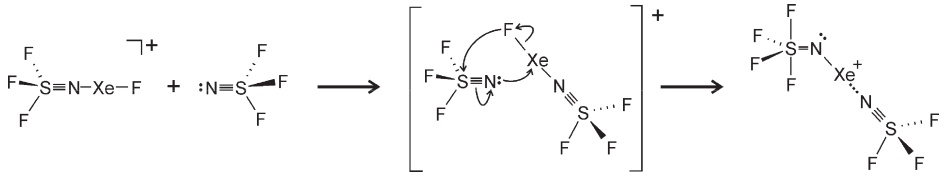

SO_2 to form the Lewis acid-base adducts $F_3S{\equiv}NBF_3$,[12,13] $F_3S{\equiv}NAsF_5$,[14,15] and $F_3S{\equiv}NSbF_5$;[14] by the formation of transition-metal complexes such as $[M(N{\equiv}SF_3)_4(AsF_6)_2]$ (M = Mn,[16] Zn[17]), $[Re(CO)_5N{\equiv}SF_3][AsF_6]$,[18] and $[CpFe(CO)_2N{\equiv}SF_3][AsF_6]$;[18] and more recently by the synthesis and structural characterization of the noble-gas-containing Lewis acid-base adduct $F_3S{\equiv}NXeF^+$.[19]

The present work investigates the reactivities of the $F_3S{\equiv}NXeF^+$ and $F_4S{=}NXe^+$ cations in $N{\equiv}SF_3$ solvent. The synthesis and detailed structural characterization of $[F_4S{=}N{-}Xe{---}N{\equiv}SF_3][AsF_6]$, a rare example of xenon bonded to an imido nitrogen and of a N−Xe−N linkage, is reported along with those of $[F_3S(N{\equiv}SF_3)_2][AsF_6]$, a reduction product resulting from the reaction of $[F_4S{=}N{-}Xe{---}N{\equiv}SF_3][AsF_6]$ with $N{\equiv}SF_3$.

Results and Discussion

Reactions of $[F_3S{\equiv}NXeF][AsF_6]$ in $N{\equiv}SF_3$ Solvent. (a) Synthesis of $[F_4S{=}N{-}Xe{---}N{\equiv}SF_3][AsF_6]$. The salt $[F_3S{\equiv}NXeF][AsF_6]$ was prepared as previously described[19] by reaction of $[XeF][AsF_6]$ with $N{\equiv}SF_3$ in neat $N{\equiv}SF_3$ at −20 °C for ca. 6 h to give a white solid, corresponding to $[F_3S{\equiv}NXeF][AsF_6]$, and a colorless supernatant. When the reaction mixture was warmed from −20 to 0 °C over ca. 15 h, the solid dissolved and the solution turned deep yellow, coinciding with the formation of $[F_4S{=}N{-}Xe{---}N{\equiv}SF_3][AsF_6]$ (eq 1). The removal of excess $N{\equiv}SF_3$ under dynamic vacuum at −50 °C yielded a deep yellow solid which was characterized by Raman spectroscopy at −160 °C. A prior study reported the ^{19}F parameters for the $F_4S{=}NXe^+$ cation in $N{\equiv}SF_3$ solvent at 0 °C;[11] however, a separate ^{19}F resonance corresponding to coordinated $N{\equiv}SF_3$ was not observed. It may be concluded that $N{\equiv}SF_3$ ligand exchange with the solvent occurs and that the donor-acceptor bond is labile under these conditions.

$$[F_3S{\equiv}NXeF][AsF_6] + N{\equiv}SF_3 \xrightarrow[N{\equiv}SF_3]{0\ ^\circ C} [F_4S{=}N{-}Xe{---}N{\equiv}SF_3][AsF_6] \quad (1)$$

The solid-state rearrangement of $F_3S{\equiv}NXeF^+$ to $F_4S{=}NXe^+$ was shown to occur at 22 °C over a period of ca. 70 min.[11] The X-ray crystal structure of $[F_3S{\equiv}NXeF][AsF_6]$[19] reveals that a fluorine ligand of AsF_6^- has a short contact (2.871(5) Å) with the sulfur atom of an adjacent $F_3S{\equiv}NXeF^+$ cation that is significantly less than the sum of the sulfur and fluorine van der Waals radii (3.27 Å).[20] In the proposed rearrangement mechanism, the short F---S contact leads to fluoride ion transfer and formation of the $[F_4S{=}NXe][AsF_6]$ ion pair.[11] As the rearrangement proceeds, solid-state dilution of $[F_3S{\equiv}NXeF][AsF_6]$ and breakdown of the crystal lattice prevent complete conversion to $[F_4S{=}NXe][AsF_6]$. In the present solution study, the rearrangement proceeds at 0 °C with complete conversion to $[F_4S{=}N{-}Xe{---}N{\equiv}SF_3][AsF_6]$. In both cases, the reactions were monitored by Raman spectroscopy (vide infra). Solvent-induced rearrangement of $F_3S{\equiv}NXeF^+$ to $F_4S{=}NXe^+$ in anhydrous HF (aHF) solution also occurs at a lower temperature (−20 °C) with complete conversion.[11] Unlike the solid-state rearrangement of $[F_3S{\equiv}NXeF][AsF_6]$,[11] rearrangements of the $F_3S{\equiv}NXeF^+$ in $N{\equiv}SF_3$ and aHF solutions do not suffer from solid-state dilution effects and proceed to completion.

Thiazyl trifluoride solvent likely promotes rearrangement at lower temperatures by means of solvent-induced S_N2 displacement of the fluoride ion from the Xe−F group, and concomitant fluoride ion coordination to sulfur (Scheme 1). An alternative mechanism in which $N{\equiv}SF_3$ accepts a fluoride ion from the Xe−F group of $F_3S{\equiv}NXeF^+$ to generate $F_4S{=}N^-$ as an intermediate seems less likely because this anion has not been experimentally observed. In the proposed solid-state and HF solution rearrangement mechanisms of $[F_3S{\equiv}NXeF][AsF_6]$ to $[F_4S{=}NXe][AsF_6]$,[11] the sulfur center is initially attacked by the coordination of fluoride from AsF_6^- and HF, respectively, followed by fluoride ion abstraction from the Xe−F group by AsF_5 and HF, respectively.

(b) Synthesis of $[F_3S(N{\equiv}SF_3)_2][AsF_6]$. In the course of growing single crystals of $[F_4S{=}N{-}Xe{---}N{\equiv}SF_3][AsF_6]$ from $N{\equiv}SF_3$ solution for an X-ray structure determination, colorless $[F_3S(N{\equiv}SF_3)_2][AsF_6]$ crystals were also obtained and characterized by single-crystal X-ray diffraction. The latter salt resulted from redox decomposition of the $F_4S{=}NXe^+$ cation at 0 °C (eq 2), and liberated Xe and N_2F_2 exclusively as the *cis*- isomer. The synthesis of pure $[F_3S(N{\equiv}SF_3)_2][AsF_6]$ was accomplished by allowing a $N{\equiv}SF_3$ solution of $[F_4S{=}N{-}Xe{---}N{\equiv}SF_3][AsF_6]$ (vide supra) to stand at 0 °C for 6 h. Over this period of time, the solution changed from yellow to colorless, accompanied by slow gas evolution. Removal of excess $N{\equiv}SF_3$ by brief pumping under dynamic vacuum at −50 °C yielded a friable white solid, comprised of

(12) Glemser, O.; Richert, H. *Z. Anorg. Allg. Chem.* **1961**, *307*, 313–327.
(13) Muller, A.; Glemser, O.; Scherf, K. *Chem. Ber.* **1966**, *99*, 3568–3571.
(14) Glemser, O.; Koch, W. *Anales. Asoc. Quim. Argentina* **1971**, *59*, 143–148.
(15) Glemser, O.; Mews, R. *Angew. Chem., Int. Ed. Engl.* **1980**, *19*, 883–899.
(16) Buss, B.; Clegg, W.; Hartmann, G.; Jones, P. G.; Mews, R.; Noltemeyer, M.; Sheldrick, G. M. *J. Chem. Soc., Dalton Trans.* **1981**, 61–63.
(17) Behrens, U.; Hoppenheit, R.; Isenberg, W.; Lork, E.; Petersen, J.; Mews, R. *Z. Naturforsch.* **1994**, *49b*, 238–242.
(18) Behrens, U.; Lork, E.; Petersen, J.; Waterfeld, A.; Mews, R. *Z. Anorg. Allg. Chem.* **1997**, *623*, 1518–1524.
(19) Smith, G. L.; Mercier, H. P. A.; Schrobilgen, G. J. *Inorg. Chem.* **2007**, *46*, 1369–1378.
(20) Bondi, A. *J. Phys. Chem.* **1964**, *68*, 441–451.

$[F_3S(N{\equiv}SF_3)_2][AsF_6]$ and *cis*-N_2F_2, which were characterized by Raman spectroscopy at −160 °C. The Raman bands assigned to *cis*-N_2F_2[21] are in excellent agreement with previously reported values.[22] Continued pumping at −45 °C for 15 min resulted in complete removal of *cis*-N_2F_2 and $N{\equiv}SF_3$ and formation of $[SF_3][AsF_6]$, which was confirmed by Raman Spectroscopy (Table S1 and Figure S1).

$$[F_4S{=}N{-}Xe{---}N{\equiv}SF_3][AsF_6] + N{\equiv}SF_3 \xrightarrow[N{\equiv}SF_3]{0\ ^\circ C} [F_3S(N{\equiv}SF_3)_2][AsF_6] + Xe + \textit{cis}\text{-}N_2F_2 \quad (2)$$

The presence of *cis*-N_2F_2 was also established in the solution ^{19}F NMR spectrum of the decomposition mixture (vide infra). The ^{19}F NMR spectrum of a $[F_3S{\equiv}NXeF][AsF_6]$ sample that had been allowed to react to completion in liquid $N{\equiv}SF_3$ solvent at 0 °C (eqs 1 and 2) showed a broad ($\Delta\nu_{1/2} = 500$ Hz) resonance at 38.6 ppm assigned to SF_3^+, in agreement with the reported value of 30.5 ppm in aHF at 25 °C.[23] The ^{19}F NMR spectrum also confirmed the formation of *cis*-N_2F_2 (singlet, 137.6 ppm, $\Delta\nu_{1/2} = 30$ Hz), in agreement with the previously reported chemical shift (broad triplet at 133.7 ppm, $^1J(^{19}F{-}^{14}N) = 145$ Hz, 25 °C, $CFCl_3$ solvent).[24] Failure to observe the $^1J(^{19}F{-}^{14}N)$ coupling in the present study is likely a consequence of quadrupolar relaxation resulting from a higher solvent viscosity and lower temperature. No *trans*-N_2F_2 was observed in the sample (broad triplet at 94.9 ppm, $^1J(^{19}F{-}^{14}N) = 136$ Hz, 25 °C, $CFCl_3$ solvent).[24] Nitrogen trifluoride was also observed by ^{19}F NMR spectroscopy (20 mol % when compared with the total molar amounts of NF_3 and *cis*-N_2F_2 soluble in the sample at 0 °C).

The proposed decomposition of $[F_4S{=}N{-}Xe{---}N{\equiv}SF_3][AsF_6]$ involves 2e reductions of xenon (+II to 0) and sulfur (+VI to +IV) and a 4e oxidation of nitrogen (−III to +I), that give Xe gas, SF_3^+, and NF radicals that combine to form *cis*-N_2F_2.[25] The series of reactions responsible for these products may be initiated by fluoride ion transfer from an AsF_6^- anion to the xenon atom of $F_4S{=}NXe^+$, forming $F_4S{=}NXeF$ as an intermediate (eq 3), which decomposes to Xe, *cis*-N_2F_2, and SF_4 (eqs 4, 5). Fluoride ion abstraction by AsF_5 generated in eq 3 leads to SF_3^+ (eq 6). Nitrogen trifluoride may result from oxidation of *cis*-N_2F_2 by $F_4S{=}NXe^+$ according to eq 7.

$$F_4S{=}NXe^+ + AsF_6^- \xrightarrow[N{\equiv}SF_3]{0\ ^\circ C} [F_4S{=}NXeF] + AsF_5 \quad (3)$$

$$[F_4S{=}NXeF] \xrightarrow[N{\equiv}SF_3]{0\ ^\circ C} \cdot NF + Xe + SF_4 \quad (4)$$

$$2\cdot NF \xrightarrow[N{\equiv}SF_3]{0\ ^\circ C} \textit{cis}\text{-}N_2F_2 \quad (5)$$

$$SF_4 + AsF_5 \xrightarrow[N{\equiv}SF_3]{0\ ^\circ C} SF_3^+ + AsF_6^- \quad (6)$$

$$F_4S{=}NXe^+ + \textit{cis}\text{-}N_2F_2 \xrightarrow[N{\equiv}SF_3]{0\ ^\circ C} NF_3 + N_2 + SF_3^+ + Xe \quad (7)$$

Table 1. Summary of Crystal Data and Refinement Results for $[F_4S{=}N{-}Xe{---}N{\equiv}SF_3][AsF_6]$ and $[F_3S(N{\equiv}SF_3)_2][AsF_6]$

	$[F_4S{=}N{-}Xe{---}N{\equiv}SF_3]$-$[AsF_6]$	$[F_3S(N{\equiv}SF_3)_2]$-$[AsF_6]$
empirical formula	$F_{13}N_2S_2XeAs$	$F_{15}N_2S_3As$
space group (no.)	$P2_1/n$ (14)	$P2_1/n$ (14)
a (Å)	7.3107(5)	7.4722(5)
b (Å)	12.0219(8)	16.264(1)
c (Å)	13.5626(9)	10.4247(7)
β (deg)	94.647(1)	97.919(1)
V (Å^3)	1188.08(1)	1254.84(3)
molecules/unit cell	4	4
mol wt (g mol^{-1})	545.36	484.12
calcd density (g cm^{-3})	3.049	2.563
T (°C)	−173	−173
μ (mm^{-1})	6.17	3.39
R_1[a]	0.0294	0.0324
wR_2[b]	0.0709	0.0633

[a] R_1 is defined as $\Sigma||F_o|-|F_c||/\Sigma|F_o|$ for $I > 2\sigma(I)$. [b] wR_2 is defined as $[\Sigma[w(F_o^2 - F_c^2)^2]/\Sigma w(F_o^2)^2]^{1/2}$ for $I > 2\sigma(I)$.

X-ray Crystal Structures of $[F_4S{=}N{-}Xe{---}N{\equiv}SF_3][AsF_6]$ and $[F_3S(N{\equiv}SF_3)_2][AsF_6]$. A summary of the refinement results and other crystallographic information are provided in Table 1. Important bond lengths and angles for $[F_4S{=}N{-}Xe{---}N{\equiv}SF_3][AsF_6]$ and $[F_3S(N{\equiv}SF_3)_2][AsF_6]$, along with calculated values (see Computational Results), are listed in Tables 2 and 3, respectively.

(a) $[F_4S{=}N{-}Xe{---}N{\equiv}SF_3][AsF_6]$. The crystal structure of $[F_4S{=}N{-}Xe{---}N{\equiv}SF_3][AsF_6]$ consists of well-separated $F_4S{=}N{-}Xe{---}N{\equiv}SF_3^+$ cations and AsF_6^- anions, with closest cation-anion contacts occurring between the equatorial fluorine F(3) of the cation and F(12) and F(14) of the anion (F(3)---F(12), 2.755(4) Å; F(3)---F(14), 2.757(4) Å), which are somewhat less than the sum of the fluorine van der Waals radii (2.94 Å).[20] The AsF_6^- anion shows little distortion from octahedral symmetry, with As−F bonds ranging from 1.713(2) to 1.735(2) Å and F−As−F bond angles ranging from 89.3(1) to 91.0(1)° and 178.8(1) to 179.2(1)°, in good agreement with previously reported values.[19,26] The ligand arrangement at the sulfur atom of the cation is a distorted

(21) The presence of *cis*-N_2F_2 was established from its Raman bands at 354(co), 729(sh), 888(co), 946(5), and 1519(co) cm^{-1}, where the abbreviations denote coincidence (co) and shoulder (sh). The bands at 354 and 888 cm^{-1} are coincident with the $[\delta(N1S1F2) + \delta(F1S1F3) + \delta(N2S2F6) + \delta(F4S2F5)]$ and $[\delta(S1F2 - S1F3) + \delta(S2F6 - S2F4)]$ bands of $F_3S(N{\equiv}SF_3)_2^+$, and the band at 1519 cm^{-1} is coincident with the $\nu(S{\equiv}N)$ band of unreacted $F_4S{=}N{-}Xe{---}N{\equiv}SF_3^+$. The presence of *cis*-$N_2F_2$ after pumping at −50 °C was surprising in view of the vapor-pressure of *cis*-N_2F_2 at −50 °C (1.19×10^4 mm Hg), suggesting it may be adducted to unreacted $F_4S{=}NXe^+$ remaining in the product mixture: Zaborowski, L. M.; De Marco, R. A.; Shreeve, J. M. *Inorg. Chem.* **1973**, *14*, 34–39.

(22) King, S.-T.; Overend, J. *Spectrochim. Acta* **1967**, *23A*, 61–66.

(23) Azeem, M.; Brownstein, M.; Gillespie, R. J. *Can. J. Chem.* **1969**, *47*, 4159–4167.

(24) Noggle, J. H.; Baldeschwieler, J. D.; Colburn, C. B. *J. Chem. Phys.* **1962**, *37*, 182–189.

(25) Diesen, R. W. *J. Chem. Phys.* **1964**, *41*, 3256–3257.

(26) Fir, B. A.; Whalen, J. M.; Mercier, H. P. A.; Dixon, D. A.; Schrobilgen, G. J. *Inorg. Chem.* **2006**, *45*, 1978–1996.

Table 2. Experimental Geometry for $[F_4S{=}N{-}Xe{-}{-}{-}N{\equiv}SF_3][AsF_6]$ and Calculated Geometries for $F_4S{=}N{-}Xe{-}{-}{-}N{\equiv}SF_3^+$ [a]

bond lengths (Å)

		calcd[b]				
	exptl	MP2	PBE1PBE	B3LYP		exptl
Xe(1)−N(1)	2.079(3)	2.062	2.079	2.131	As(1)−F(8)	1.726(2)
N(1)=S(1)	1.539(3)	1.563	1.557	1.573	As(1)−F(9)	1.714(2)
S(1)−F(1)	1.586(3)	1.576	1.577	1.593	As(1)−F(10)	1.722(2)
S(1)−F(2)	1.520(3)	1.545	1.544	1.558	As(1)−F(11)	1.721(2)
S(1)−F(3)	1.529(3)	1.545	1.544	1.558	As(1)−F(12)	1.718(2)
S(1)−F(4)	1.577(3)	1.619	1.611	1.625	As(1)−F(13)	1.735(2)
Xe(1)---N(2)	2.583(3)	2.524	2.547	2.623		
N(2)≡S(2)	1.398(3)	1.428	1.413	1.417		
S(2)−F(5)	1.524(3)	1.545	1.541	1.558		
S(2)−F(6)	1.521(3)	1.545	1.541	1.558		
S(2)−F(7)	1.526(3)	1.545	1.541	1.559		

bond angles (deg)

		calcd[b]				
	exptl	MP2	PBE1PBE	B3LYP		exptl
Xe(1)−N(1)=S(1)	119.8(2)	119.3	119.8	119.8	F(8)−As(1)−F(9)	179.0(1)
N(1)=S(1)−F(1)	87.6(2)	88.1	87.9	87.3	F(8)−As(1)−F(10)	89.6(1)
N(1)=S(1)−F(2)	126.4(2)	127.1	126.8	127.0	F(8)−As(1)−F(11)	89.7(1)
N(1)=S(1)−F(3)	128.2(2)	127.1	126.8	127.0	F(8)−As(1)−F(12)	90.4(1)
N(1)=S(1)−F(4)	99.7(1)	98.8	99.1	99.1	F(8)−As(1)−F(13)	89.3(1)
F(1)−S(1)−F(2)	88.0(2)	88.7	88.6	88.7	F(9)−As(1)−F(10)	90.3(1)
F(1)−S(1)−F(3)	87.2(1)	88.7	88.6	88.7	F(9)−As(1)−F(11)	90.4(1)
F(1)−S(1)−F(4)	172.7(1)	173.1	173.0	173.6	F(9)−As(1)−F(12)	90.6(1)
F(2)−S(1)−F(3)	104.9(1)	105.7	106.1	105.6	F(9)−As(1)−F(13)	89.8(1)
F(2)−S(1)−F(4)	88.2(1)	87.1	87.2	87.4	F(10)−As(1)−F(11)	178.8(1)
F(3)−S(1)−F(4)	87.7(1)	87.1	87.2	87.4	F(10)−As(1)−F(12)	91.0(1)
N(1)−Xe(1)---N(2)	168.4(1)	173.2	173.5	173.1	F(10)−As(1)−F(13)	89.7(1)
Xe(1)---N(2)≡S(2)	148.0(2)	178.6	178.3	178.6	F(11)−As(1)−F(12)	90.0(1)
N(2)≡S(2)−F(5)	120.4(2)	121.1	120.9	121.1	F(11)−As(1)−F(13)	89.4(1)
N(2)≡S(2)−F(6)	122.8(2)	121.2	121.1	121.3	F(12)−As(1)−F(13)	179.2(1)
N(2)≡S(2)−F(7)	120.9(2)	121.3	121.1	121.3		
F(5)−S(2)−F(6)	95.5(2)	95.6	95.8	95.5		
F(5)−S(2)−F(7)	95.2(2)	95.6	95.8	95.5		
F(6)−S(2)−F(7)	95.5(2)	95.6	95.8	95.6		

[a] The atom labels correspond to those used in Figure 1. [b] aug-cc-pVTZ(-PP) basis set.

trigonal bipyramid, with the nitrogen and two fluorine atoms occupying the equatorial plane and two axial fluorine atoms approximately perpendicular to that plane (Figure 1a). The xenon atom is coplanar with the orthogonal plane defined by the N, S, and axial F atoms, and the Xe−N=S angle is bent (119.8(2)°) as a result of the sterically active valence electron lone pair on nitrogen.

The Xe−N(1) bond length (2.079(3) Å) is equal, within $\pm 3\sigma$, to those of $[F_4S{=}NXe][AsF_6]$ (2.083(3) Å)[11] and $[F_5SN(H)Xe][AsF_6]$ (2.069(4) Å),[27] somewhat longer than the Xe−N bond of $[F_5TeN(H)Xe][AsF_6]$ (2.044(4) Å),[26] but considerably shorter than the Xe−N bonds of nitrogen base adducts of XeF^+ (vide infra). The S=N bond length of $F_4S{=}N{-}Xe{-}{-}{-}N{\equiv}SF_3^+$ (1.539(3) Å) is also equal, within experimental error, to those of $[F_4S{=}NXe][AsF_6]$ (1.556(3) Å)[11] and $F_4S{=}NF$ (1.520(9) Å)[28] but is longer than those of $F_4S{=}NH_2^+$ (1.511(6) Å)[11] and $F_4S{=}NCH_3$ (1.480(6) Å).[29] All of the SF_4-group bond lengths of $F_4S{=}N{-}Xe{-}{-}{-}N{\equiv}SF_3^+$ are the same within $\pm 3\sigma$ as those of $[F_4S{=}NXe][AsF_6]$.[11] The Xe−N(1)=S(1) and N(1)=S(1)−F(1) angles of $F_4S{=}N{-}Xe{-}{-}{-}N{\equiv}SF_3^+$ (119.8(2) and 87.6(2)°) are slightly greater than those of $[F_4S{=}NXe][AsF_6]$ (118.0(2) and 86.4(2)°).[11] All other angles that are in common with the two structures are equal within ±0.9°. Comparisons of $F_4S{=}NXe^+$ with $F_4S{=}NH_2^+$, $F_4S{=}NCH_3$, and $F_4S{=}NF$ have been discussed in detail in ref 11.

The short Xe---N(2) contact (2.583(3) Å) is well within the sum of the nitrogen and xenon van der Waals radii (3.71 Å)[20] but considerably longer than the Xe−N bond lengths of the related cations $[F_3S{\equiv}NXeF][AsF_6]$ (2.236(4) Å),[19] $[HC{\equiv}NXeF][AsF_6]$ (2.235(3) Å),[30] $[(CH_3)_3C{\equiv}NXeF][AsF_6]$ (2.212(4) Å),[30] and $[CH_3C{\equiv}NXeF][AsF_6]{\cdot}HF$ (2.179(7) Å),[30] while somewhat shorter than the Xe---N contacts in the $CH_3C{\equiv}N$ solvated salts of the more weakly acidic $C_6F_5Xe^+$ cation, $[C_6F_5Xe{-}{-}{-}N{\equiv}CCH_3][B(C_6F_5)_4]$ (2.610(11) Å),[31] $[C_6F_5Xe{-}{-}{-}N{\equiv}CCH_3][B(CF_3)_4]$ (2.640(6) Å),[31] $[C_6F_5Xe{-}{-}{-}N{\equiv}CCH_3][(C_6F_5)_2BF_2]$

(27) Smith, G. L.; Mercier, H. P. A.; Schrobilgen, G. J. *Inorg. Chem.* **2008**, *47*, 4173–4184.
(28) DesMarteau, D. D.; Eysel, H. H.; Oberhammer, H.; Günther, H. *Inorg. Chem.* **1982**, *21*, 1607–1616.
(29) Günther, H.; Oberhammer, H.; Mews, R.; Stahl, I. *Inorg. Chem.* **1982**, *21*, 1872–1875.
(30) Fir, B. A. M. Sc. Thesis, McMaster University, Hamilton, ON, **1999**.
(31) Koppe, K.; Frohn, H.-J.; Mercier, H. P. A.; Schrobilgen, G. J. *Inorg. Chem.* **2008**, *47*, 3205–3217.

Table 3. Experimental and Calculated Geometries for $[F_3S(N{\equiv}SF_3)_2][AsF_6]$[a]

bond lengths (Å)

		calcd[b]				calcd[b]	
	exptl	PBE1PBE	B3LYP		exptl	PBE1PBE	B3LYP
S(3)−F(7)	1.511(1)	1.557	1.573	S(3)--N(1)	2.554(2)	2.610	2.689
S(3)−F(8)	1.519(1)	1.544	1.555	N(1)−S(1)	1.384(2)	1.416	1.421
S(3)−F(9)	1.520(1)	1.544	1.555	S(1)−F(1)	1.518(2)	1.562	1.580
S(3)--F(10)	2.558(2)	2.223	2.217	S(1)−F(2)	1.521(1)	1.545	1.566
As(1)−F(10)	1.745(1)	1.832	1.863	S(1)−F(3)	1.518(2)	1.552	1.570
As(1)−F(11)	1.723(1)	1.743	1.756	S(3)--N(2)	2.511(2)	2.610	2.689
As(1)−F(12)	1.708(2)	1.728	1.741	N(2)−S(2)	1.392(2)	1.416	1.421
As(1)−F(13)	1.684(2)	1.705	1.717	S(2)−F(4)	1.516(2)	1.552	1.570
As(1)−F(14)	1.706(1)	1.706	1.719	S(2)−F(5)	1.525(2)	1.562	1.580
As(1)−F(15)	1.714(2)	1.728	1.741	S(2)−F(6)	1.525(2)	1.548	1.566

bond angles (deg)

		calcd[b]				calcd[b]	
	exptl	PBE1PBE	B3LYP		exptl	PBE1PBE	B3LYP
F(7)−S(3)−F(8)	96.2(1)	94.5	94.4	F(10)−As(1)−F(11)	88.2(1)	86.6	86.3
F(7)−S(3)−F(9)	96.8(1)	94.5	94.4	F(10)−As(1)−F(12)	87.9(1)	87.1	86.9
F(8)−S(3)−F(9)	96.3(1)	95.0	95.5	F(10)−As(1)−F(13)	179.0(1)	178.6	178.6
F(7)−S(3)--F(10)	174.3(1)	174.9	175.4	F(10)−As(1)−F(14)	89.7(1)	87.6	87.3
F(7)−S(3)--N(1)	83.1(1)	83.9	84.5	F(10)−As(1)−F(15)	87.4(1)	87.1	86.9
F(7)−S(3)--N(2)	81.1(1)	83.9	84.4	F(11)−As(1)−F(12)	89.8(1)	88.4	88.4
F(8)−S(3)--F(10)	78.4(1)	82.1	82.5	F(11)−As(1)−F(13)	91.1(1)	92.0	92.3
F(8)−S(3)--N(1)	83.2(1)	79.4	79.2	F(11)−As(1)−F(14)	177.8(1)	174.2	173.5
F(8)−S(3)--N(2)	177.3(1)	174.0	174.5	F(11)−As(1)−F(15)	89.2(1)	88.4	88.4
F(9)−S(3)--F(10)	82.3(1)	82.1	82.5	F(12)−As(1)−F(13)	92.9(1)	92.9	93.1
F(9)−S(3)--N(1)	179.5(1)	174.0	174.5	F(12)−As(1)−F(14)	89.8(1)	91.3	91.2
F(9)−S(3)--N(2)	84.2(1)	79.4	79.2	F(12)−As(1)−F(15)	175.2(1)	173.4	173.1
F(10)--S(3)--N(1)	97.7(1)	99.1	98.3	F(13)−As(1)−F(14)	91.0(1)	93.8	94.1
F(10)--S(3)--N(2)	104.4(1)	99.1	98.3	F(13)−As(1)−F(15)	91.9(1)	92.9	93.1
N(1)--S(3)--N(2)	96.3(1)	106.1	106.0	F(14)−As(1)−F(15)	91.0(1)	91.3	91.2
S(3)--N(1)−S(1)	158.3(1)	141.5	142.7	S(3)--N(2)−S(2)	132.2(1)	141.6	142.7
N(1)−S(1)−F(1)	121.7(1)	119.4	119.7	N(2)−S(2)−F(4)	121.8(1)	122.8	122.9
N(1)−S(1)−F(2)	121.9(1)	123.6	123.7	N(2)−S(2)−F(5)	120.2(1)	119.4	119.7
N(1)−S(1)−F(3)	120.9(1)	122.8	122.9	N(2)−S(2)−F(6)	122.2(1)	123.6	123.7
F(1)−S(1)−F(2)	95.3(1)	94.2	94.0	F(4)−S(2)−F(5)	95.2(1)	94.3	94.1
F(1)−S(1)−F(3)	95.3(1)	94.3	94.1	F(4)−S(2)−F(6)	95.2(1)	95.2	95.0
F(2)−S(1)−F(3)	94.8(1)	95.2	95.0	F(5)−S(2)−F(6)	95.5(1)	94.2	94.0

[a] The atom labels correspond to those used in Figure 2. [b] Calculated for the gas-phase ion-pair using the aug-cc-pVTZ(-PP) basis set.

(2.681(8) Å),[32] and $[C_6F_5Xe{-}{-}{-}NC_5H_3F_2][AsF_6]$ (2.694(5) Å).[33] The donor-acceptor bond length trends are in accordance with the gas-phase donor-acceptor dissociation energies calculated for $F_3S{\equiv}NXeF^+$, $HC{\equiv}NXeF^+$, $F_4S{=}N{-}Xe{-}{-}{-}N{\equiv}SF_3^+$, and $F_3S{\equiv}NAsF_5$ (see Computational Results).

The bent Xe---N≡S angle (148.0(2)°) is similar to that of $[F_3S{\equiv}NXeF][AsF_6]$ (142.6(3)°)[19] and to the Xe---N≡C angles in $[C_6F_5Xe{-}{-}{-}N{\equiv}CCH_3][B(C_6F_5)_4]$ (150.3(9)°)[31] and $[C_6F_5Xe{-}{-}{-}N{\equiv}CCH_3][B(CF_3)_4]$ (155.0(7)°)[31] but contrasts with the nearly linear Xe---N≡C angles in $[HC{\equiv}NXeF][AsF_6]$ (177.7(3)°),[30] $[CH_3C{\equiv}NXeF][AsF_6]{\cdot}HF$ (175.0(8)°),[30] and $[(CH_3)_3C{\equiv}NXeF][AsF_6]$ (166.9(4)°)[30] and with the near-linear gas-phase geometries predicted by quantum-chemical calculations (MP2/aug-cc-pVTZ(-PP)) for the gas-phase ions. The N−Xe---N angle (168.4(1)°) deviates somewhat more from linearity than the C−Xe---N angles of $[C_6F_5Xe{-}{-}{-}N{\equiv}CCH_3][(C_6F_5)_2BF_2]$ (174.5(3)°),[32] $[C_6F_5Xe{-}{-}{-}N{\equiv}CCH_3][B(CF_3)_4]$ (174.9(2)°),[31] and $[C_6F_5Xe{-}{-}{-}N{\equiv}CCH_3][B(C_6F_5)_4]$ (176.9(3)°).[31] The out-of-plane and in-plane N−Xe---N bending frequencies are assigned at 144 and 255 cm^{-1}, respectively, and the Xe---N≡S bends, which were too low in frequency to be observed in the Raman spectrum, were calculated at 64 and 72 cm^{-1}, respectively, showing that these angles are highly deformable and that their nonlinearities likely arise from crystal packing (see Computational Results).

The bond lengths of adducted $N{\equiv}SF_3$ in $F_4S{=}N{-}Xe{-}{-}{-}N{\equiv}SF_3^+$ (S≡N, 1.398(3) and S−F, av., 1.524(3) Å) are shorter than those in free $N{\equiv}SF_3$ (S≡N, 1.415(3) and S−F, av., 1.547(1) Å).[34,35] Similar S≡N and S−F bond length

(32) Frohn, H.-J.; Jakobs, S.; Henkel, G. *Angew. Chem., Int. Ed. Engl.* **1989**, *28*, 1506–1507.

(33) Frohn, H. J.; Schroer, T.; Henkel, G. *Z. Naturforsch.* **1995**, *50b*, 1799–1810.

(34) Borrmann, T.; Lork, E.; Mews, R.; Parsons, S.; Petersen, J.; Stohrer, W.-D.; Watson, P. G. *Inorg. Chim. Acta* **2008**, *361*, 479–486.

(35) The geometrical parameters of $N{\equiv}SF_3$ have also been determined by microwave spectrocopy: d(N−S) = 1.416(3) Å; d(S−F) = 1.552(3) Å; ∠FSF = 94.0(3)°; ∠NSF = 122.4(3)° [Kirchhoff, W. H.; Wilson, E. B., Jr. *J. Am. Chem. Soc.* **1962**, *84*, 334–336.] The recently published low-temperature X-ray crystal structure was obtained at −153 °C,[34] which is similar to the data collection temperature used for the present work (−173 °C). Moreover, the X-ray crystal structure is more precise than the microwave structure and is used for comparison in the present discussion.

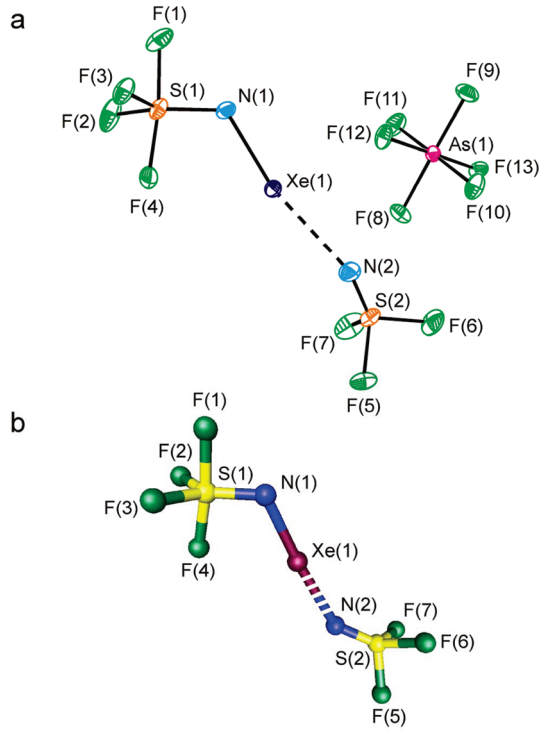

Figure 1. (a) The structural unit in the X-ray crystal structure of $[F_4S{=}N{-}Xe{-}{-}{-}N{\equiv}SF_3][AsF_6]$. Thermal ellipsoids are shown at the 50% probability level. (b) The gas-phase geometry of the $F_4S{=}N{-}Xe{-}{-}{-}N{\equiv}SF_3^+$ cation calculated at the MP2/aug-cc-pVTZ level of theory (Table 2).

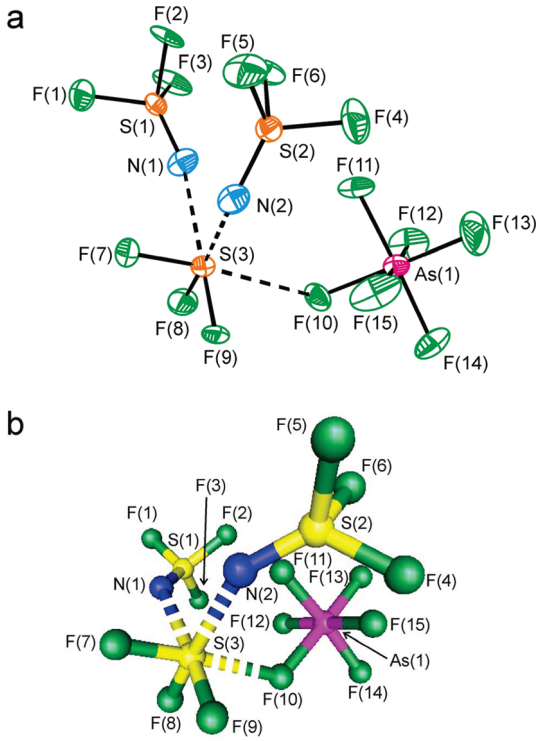

Figure 2. (a) The structural unit in the X-ray crystal structure of $[F_3S(N{\equiv}SF_3)_2][AsF_6]$. Thermal ellipsoids are shown at the 50% probability level. (b) The gas-phase geometry of $[F_3S(N{\equiv}SF_3)_2][AsF_6]$ calculated at the PBE1PBE/aug-cc-pVTZ level of theory (Table 3).

contractions have been observed in other main-group adducts,[15] namely, $F_3S{\equiv}NAsF_5$ (1.383 and 1.439 Å)[15] and $[F_3S{\equiv}NXeF][AsF_6]$ (1.397(5) and 1.503(3) Å),[19] and in the transition metal adducts $[Mn(N{\equiv}SF_3)_4][AsF_6]_2$ (1.365(11) and 1.506(5) Å)[16] and $[Re(CO)_5N{\equiv}SF_3][AsF_6]$ (1.384(14) and 1.499(10) Å;[36] see Computational Results).

The N≡S−F and F−S−F angles in the adducted $N{\equiv}SF_3$ molecule average 121.4(2)° and 95.4(2)°, respectively, comprising a distorted tetrahedral arrangement about sulfur that is similar to those of free $N{\equiv}SF_3$ (av., 122.2(2)° and 94.2(1)°),[34] and of adducted $N{\equiv}SF_3$, as in $F_3S{\equiv}NAsF_5$ (122.2° and 94.3°)[15] and $[F_3S{\equiv}NXeF][AsF_6]$ (av., 119.8(2) and 97.4(2) Å;[19] also see Computational Results).

(b) $[F_3S(N{\equiv}SF_3)_2][AsF_6]$. The SF_3^+ cation has been previously characterized as its AsF_6^-,[23,37−40] SbF_6^-,[23,37] PF_6^-,[23,39] BF_4^-,[23,37−39] and GeF_6^{2-} [41] salts. A series of mixed CF_3/F adduct cations, $[(CF_3)_n(F)_{3-n}S{-}{-}{-}N{\equiv}SF_3][AsF_6]$ ($n = 0{-}2$), has been studied by ^{19}F NMR spectroscopy in SO_2 solvent at temperatures below −30 °C where the cations corresponding to $n = 0$ or 1 are labile and weakly coordinated.[42] In contrast, the $(CF_3)_2FS{-}{-}{-}N{\equiv}SF_3^+$ cation is nonlabile and pentacoordinate at sulfur in SO_2 solvent at temperatures below −30 °C.

The crystal structure of $[F_3S(N{\equiv}SF_3)_2][AsF_6]$ consists of an SF_3^+ cation having three long contacts to S(IV), one to a fluorine atom of a neighboring AsF_6^- anion, and two to the nitrogen atoms of the $N{\equiv}SF_3$ molecules (Figure 2). Ignoring the S---N and S---F contacts, the SF_3^+ cation is very close to C_{3v} symmetry, as has been observed for $[SF_3][BF_4]$[38] and $[SF_3]_2[GeF_6]$,[41] the only other SF_3^+ salts to have been structurally characterized by single-crystal X-ray diffraction. In the latter salts, the S(IV) coordination sphere includes three long contacts to fluorine ligands of their anions.[38] As in the $[SF_3][BF_4]$ and $[SF_3]_2[GeF_6]$ salts, the arrangement of long contacts in the present structure avoids, to the maximum extent, the F atoms and the nonbonding electron pair situated on the pseudo-3-fold axis opposite the F ligands of SF_3^+, providing distorted octahedral coordination at the S(IV) atom.

The S−F bond lengths of SF_3^+ (1.511(1), 1.519(1), 1.520(1) Å) in $[F_3S(N{\equiv}SF_3)_2][AsF_6]$ are equal, within experimental error, to those in $[SF_3]_2[GeF_6]$ (1.515(2), 1.519(2), 1.519(2) Å)[41] and are somewhat longer than those in $[SF_3][BF_4]$ (1.495(2), 1.495(2), 1.499(2) Å), but are within $\pm 3\sigma$ for the thermally corrected values of the latter salt (1.518, 1.518, 1.514 Å).[38] The F−S−F bond angles of the cation (96.2(1)°, 96.3(1)°, 96.8(1)°) are in agreement with those in $[SF_3]_2[GeF_6]$ (96.2(1)°)[41] and $[SF_3][BF_4]$ (97.62(7)°, 97.62(7)°, 97.39(12)°)[38] and are significantly greater than 90°, as is predicted for the gas-phase cation (94.5°, 94.5°, 95.0°; also see Computational Results). The short S---F contact between the cation and a fluorine of AsF_6^- (2.558(2) Å) of $[F_3S(N{\equiv}SF_3)_2][AsF_6]$ is well within the sum of the sulfur and fluorine van der Waals radii (3.27 Å)[20] and is bracketed by the S---F

(36) Schnepel, F. M.; Mews, R.; Glemser, O. *J. Mol. Struct.* **1980**, *60*, 89–92.
(37) Bartlett, N.; Robinson, P. L. *J. Chem. Soc.* **1961**, 3417–3425.
(38) Gibler, D. D.; Adams, C. J.; Fischer, M.; Zalkin, A.; Bartlett, N. *Inorg. Chem.* **1972**, *11*, 2325–2329.
(39) Brownstein, M.; Shamir, J. *Appl. Spectrosc.* **1972**, *26*, 77–80.
(40) Barr, M. R.; Dunell, B. A. *Can. J. Chem.* **1970**, *48*, 895–903.
(41) Mallouk, T. E.; Rosenthal, G. R.; Müller, G.; Brusasco, R.; Bartlett, N. *Inorg. Chem.* **1984**, *23*, 3167–3173.
(42) Erhart, M.; Mews, R. *Z. Anorg. Allg. Chem.* **1992**, *615*, 117–122.

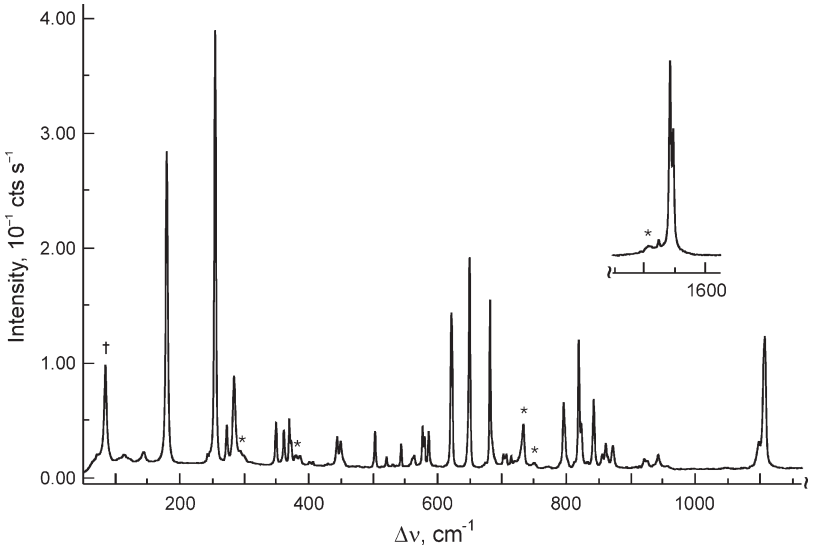

Figure 3. The Raman spectrum of $[F_4S{=}N{-}Xe{-}{-}{-}N{\equiv}SF_3][AsF_6]$ recorded at −160 °C using 1064-nm excitation. Symbols denote FEP sample tube lines (*) and an instrumental artifact (†).

contact distances reported for $[SF_3]_2[GeF_6]$ (2.367(2) and 2.420(1) Å)[41] and for $[SF_3][BF_4]$ (2.593(3) and 2.624(2) Å).[38] The short S---N contacts between SF_3^+ and the nitrogen atoms of the $N{\equiv}SF_3$ molecules (2.511(2) and 2.554(2) Å) are significantly less than the sum of the sulfur and nitrogen van der Waals radii (3.35 Å)[20] and are similar to the S---F contact distances. The N---S---N (96.3(1)°) and F---S---N (97.7(1) and 104.4°) angles are significantly greater than 90°, forming a distorted octahedral geometry about sulfur such that the contacts to $N{\equiv}SF_3$ and AsF_6^- avoid the stereochemically active valence electron lone pair and fluorine ligands of SF_3^+ to the maximum extent and are similar to the long contacts observed in the X-ray crystal structures of $[SF_3][BF_4]$[38] and $[SF_3]_2[GeF_6]$.[41]

The bond lengths and angles of the adducted $N{\equiv}SF_3$ molecules (S≡N, 1.384(2) and 1.392(2); S−F, av., 1.520(2) Å; N−S−F, av., 121.4(1)°; F−S−F, av., 95.2(1)°) show the expected contractions[15] relative to those of free $N{\equiv}SF_3$ (S≡N, 1.415(3); S−F, av., 1.547(1) Å; N−S−F, 122.2(1)°;, F−S−F, 94.2(1)°)[34] and are very similar to those of adducted $N{\equiv}SF_3$ in $F_4S{=}N{-}Xe{-}{-}{-}N{\equiv}SF_3^+$ and in related adducts (vide supra).

Raman Spectroscopy. (a) $[F_4S{=}N{-}Xe{-}{-}{-}N{\equiv}SF_3][AsF_6]$. The Raman spectrum of the $F_4S{=}N{-}Xe{-}{-}{-}N{\equiv}SF_3^+$ cation in its AsF_6^- salt (Figure 3) was assigned by comparison with those of $[F_4S{=}NXe][AsF_6]$,[11] $N{\equiv}SF_3$,[19] and $[F_3S{\equiv}NXeF][AsF_6]$,[19] as well as by comparison with the calculated frequencies for the gas-phase energy-minimized geometries of $F_4S{=}NXe^+$,[11] $F_4S{=}NF$,[11] $F_3S{\equiv}NXeF^+$,[19] $N{\equiv}SF_3$,[19] and $F_4S{=}N{-}Xe{-}{-}{-}N{\equiv}SF_3^+$ (see Table 4, Computational Results). The vibrational modes of the uncoordinated AsF_6^- anion were assigned by comparison with those of $[O_2][AsF_6]$,[43] $[HC{\equiv}NXeF][AsF_6]$,[44] $[F_3S{\equiv}NXeF][AsF_6]$,[19] $[F_5TeNH_3][AsF_6]$,[26] and $[F_5SNH_3][AsF_6]$.[27] Calculated frequencies at the MP2/aug-cc-pVTZ(-PP) level of theory provided the best overall agreement with experimental values (see Computational Results) and are considered in the ensuing discussion (indicated in square brackets).

The $F_4S{=}N{-}Xe{-}{-}{-}N{\equiv}SF_3^+$ cation possesses C_1 symmetry for the calculated gas-phase and X-ray structures, which is predicted to give rise to 30 Raman- and infrared-active fundamental vibrational modes belonging to A irreducible representations. The AsF_6^- anion possesses 15 fundamental vibrational modes, which were assigned under O_h symmetry and belong to the irreducible representations $A_{1g} + E_g + T_{2g} + 2T_{1u} + T_{2u}$, where the A_{1g}, E_g, and T_{2g} modes are Raman-active and the T_{1u} modes are infrared-active. The formally Raman-inactive T_{1u} modes were, however, observed as weak bands at 702, 707, 714, and 720 cm^{-1} and at 401, 403, and 407 cm^{-1}, and the formally Raman-inactive T_{2u} mode was observed as a pair of weak bands at 243 and 246 cm^{-1} (vide infra), which are accounted for in the factor-group analysis of this salt. A factor-group analysis for this salt is provided in Table S2 and is discussed in the Supporting Information.

The calculated vibrational frequencies for the $F_4S{=}N{-}Xe{-}{-}{-}N{\equiv}SF_3^+$ adduct cation are in good agreement with the experimental frequencies. The ν(Xe−N) stretch at 284 [282] cm^{-1} is slightly higher in frequency than the terminal ν(Xe−N) stretches observed for $F_4S{=}NXe^+$ (253, 259 cm^{-1})[11] and $F_5SN(H)Xe^+$ (224 cm^{-1})[27] and the ν(Xe−N) stretch in $[F_3S{\equiv}NXeF][AsF_6]$ (194 cm^{-1}).[19] The ν(Xe---N) stretch at 113 [103] cm^{-1} is considerably lower than those mentioned above but is most similar to that in $F_3S{\equiv}NXeF^+$, affirming the highly ionic character of the Xe---N donor-acceptor bond. These ν(Xe−N) and ν(Xe---N) stretching frequencies are considerably lower than the coupled ν(Xe−N) + ν(Xe−N) and ν(Xe−N) − ν(Xe−N) stretches in $Xe[N(SO_2F)_2]_2$ (413 and 406 cm^{-1} and 386 and 380 cm^{-1}, respectively).[6] The latter modes occur at higher frequencies due to the greater covalent characters of the Xe−N bonds. The in-plane and out-of-plane N−Xe---N bends in the Raman spectrum of $[F_4S{=}N{-}Xe{-}{-}{-}N{\equiv}SF_3][AsF_6]$ occur at 255 [251] and 144 [119] cm^{-1}, respectively, compared with bands observed at 201 and 161 cm^{-1} for δ(N−Xe−N) in $Xe[N(SO_2F)_2]_2$.[6] The in-plane N−Xe−N and N−Xe---N

(43) Naulin, C.; Bougon, R. *J. Chem. Phys.* **1976**, *64*, 4155–4158.
(44) Emara, A. A. A.; Schrobilgen, G. J. *Inorg. Chem.* **1992**, *31*, 1323–1332.

Table 4. Experimental Raman Frequencies and Intensities for $[F_4S{=}N{-}Xe{-}{-}{-}N{\equiv}SF_3][AsF_6]$ and Calculated Vibrational Frequencies, Intensities, and Assignments for $F_4S{=}N{-}Xe{-}{-}{-}N{\equiv}SF_3^+$

freq, cm^{-1}					
	calcd[b]			assgnts[c]	
exptl[a]	MP2	PBE1PBE1	B3LYP	$F_4S{=}NXe{-}{-}{-}N{\equiv}SF_3^+$ (C_1)	AsF_6^- (O_h)
1548 (29) 1543 (45)	1546 [350]	1601 (166) [460]	1560 (180) [408]	ν(S≡N)	
1109 (30) 1099 (6)	1132 [558]	1112 (104) [571]	1044 (145) [523]	ν(S=N)	
943 (3)	932 [181]	935 (3) [184]	893 (4) [179]	ν(S1F2 – S1F3)	
926 (2) 921 (2)	885 [303]	898 (5) [199]	848 (8) [282]	ν(S2F5 + S2F6) – ν(S2F7) + ν(S1F1) – ν(S1F4)	
872 (5)	885 [182]	897 (5) [177]	848 (6) [179]	ν(S2F5 – S2F6) + ν(S2F7)	
862 (5) 856 (3)	884 [170]	889 (19) [274]	846 (21) [185]	ν(S1F1 – S1F4) + ν(S2F7)	
824 (10) 819 (29)	823 [143]	840 (59) [151]	794 (59) [164]	ν(S2F5 + S2F6 + S2F7) + ν(S≡N)	
798 sh 796 (15)	805 [121]	799 (16) [106]	753 (18) [101]	ν(S1F2 + S1F3 + S1F4) + ν(S=N)	
720 (2) 714 (3) 707 (3) 702 (3)					[ν_3 (T_{1u})]
685 (6) 682 (38)					[ν_1 (A_{1g})]
650 (48)	659 [15]	645 (60) [37]	624 (31) [39]	δ(N=SF2F3) o.o.p.	
622 (32)	624 [6]	632 (20) [2]	604 (48) [6]	ν(S1F1 + S1F4)	
586 (8) 580 (7)					[ν_2 (E_g)]
577 (10)	578 [31]	572 (8) [44]	552 (7) [40]	δ(N=SF1) – δ(N=SF4) + ρ_w(F2S1F3)	
564 (3) 561 (2)	556 [67]	555 (1) [74]	535 (1) [87]	δ(F1S1F4) + δ(F2S1F3)	
544 (5)	527 [8]	525 (3) [7]	508 (2) [7]	δ($S2F_3$)	
531 (1) 521 (2)	511 [<1]	508 (1) [<1]	489 (1) [<1]	δ(F1S1F2) + δ(F3S1F4)	
503 (8)	496 [15]	498 (3) [16]	478 (3) [15]	δ(N=SF1F4) o.o.p. + ρ_r(F2S1F3)	
450 (6)	432 [13]	439 (4) [16]	419 (4) [14]	δ(N≡SF5F7)	
444 (7)	431 [13]	439 (4) [16]	419 (4) [13]	δ(N≡SF5F6)	
407 (1) 403 (1) 401 (1)					[ν_4 (T_{1u})]
373 sh 370 (11)					[ν_5 (T_{2g})]
362 (8)	342 [3]	341 (2) [2]	329 (2) [2]	δ(N≡SF5) + δ(F6S2F7)	
349 (10)	341 [2]	341 (2) [2]	328 (2) [2]	δ(N≡SF7) + δ(F5S2F6)	
284 (20)	282 [11]	275 (36) [8]	259 (25) [4]	ν(XeN1)	
273 (9)	264 [1]	265 (1) [1]	255 (1) [1]	δ(XeN=S) o.o.p. + δ(N=SF2) – δ(N=SF3)	
255 (100)	251 [<1]	247 (8) [<1]	237 (23) [<1]	δ(N1XeN2) i.p.	
246 sh 243 (2)					[ν_6 (T_{2u})]
180 (71)	180 [21]	175 (17) [18]	164 (14) [25]	δ(XeN=S) i.p.	
144 (2)	119 [1]	116 (1) [1]	107 (1) [1]	δ(N1XeN2) o.o.p.	
113 (2)	103 [33]	96 (<1) [34]	86 (<1) [31]	ν(XeN2)	
n.o.	72 [2]	68 (<1) [2]	60 (<1) [2]	δ(XeN≡S) i.p.	
n.o.	64 [1]	60 (<1) [1]	55 (<1) [1]	δ(XeN≡S) o.o.p.	
n.o.	20 [<1]	18 (<1) [<1]	18 (<1) [<1]	ρ_w(N≡SF_3) o.o.p.[d]	
n.o.	19 [<1]	17 (<1) [<1]	16 (<1) [<1]	ρ_w(N≡SF_3) i.p.[d]	
n.o.	2 [<1]	2 (<1) [<1]	6 (<1) [<1]	N≡SF_3 torsion about Xe---N bond	

[a] Values in parentheses denote experimental Raman intensities; abbreviations denote shoulder (sh) and not observed (n.o.). [b] The aug-cc-pVTZ(-PP) basis set. Calculated Raman intensities (in $Å^4$ amu^{-1}) are given in parentheses, and calculated infrared intensities (in km mol^{-1}) are given in brackets. Calculated Raman intensities at the MP2 level were not possible given the presently available computing resources. [c] The atom numbering corresponds to that given in Figure 1. Abbreviations denote out of plane (o.o.p.) and in plane (i.p.), where the planes are defined by the atoms they contain, unless otherwise specified; inversion (inv), wag (ρ_w), and rock (ρ_r). [d] The plane is defined by the S1, N1, and Xe1 atoms.

bends are the most intense bands in their respective Raman spectra. The out-of-plane and in-plane Xe−N=S bends of the $F_4S{=}NXe{-}$ moiety of $F_4S{=}N{-}Xe{-}{-}{-}N{\equiv}SF_3^+$ at 273 [264] and 180 [180] cm^{-1}, respectively, are in good agreement with the corresponding frequencies observed for $[F_4S{=}NXe][AsF_6]$[11] at 273, 178, and 184 cm^{-1}. Together, these values bracket the Xe−N−S bending frequencies reported for $XeN(SO_2F)_2^+$ (226, 241, 251, 259, 267 cm^{-1})[7] and $F[XeN(SO_2F)_2]_2^+$ (208, 224, 231, 240, 247, 260, 264 cm^{-1})[7] and are higher in frequency than those in $FXeN(SO_2F)_2$ (96, 111, 116, 119 cm^{-1}).[5] The S=N stretch at 1099 and 1109 [1132] cm^{-1} compares well with the S=N stretching frequencies of other imido species ($[F_4S{=}NXe][AsF_6]$, 1097, 1104 cm^{-1},[11] $F_4S{=}NF$, 1125 cm^{-1};[28] $F_4S{=}NSF_5$, 1299 cm^{-1} [45]). The experimental SF_4 stretching (622−943 cm^{-1}) and bending (503−577 cm^{-1}) frequencies fall into ranges that are similar to those of $[F_4S{=}NXe][AsF_6]$[11] and the benchmark, $F_4S{=}NF$[11,28] (see Computational Results).

(45) Waterfeld, A.; Mews, R. *Angew. Chem., Int. Ed. Engl.* **1982**, *21*, 354.

All N≡SF_3 modes of [F_4S=N−Xe---N≡SF_3][AsF_6] exhibit high-frequency shifts relative to those of N≡SF_3. The S≡N stretching mode occurs at 1543 and 1548 [1546] cm^{-1} compared to that of N≡SF_3 (solid, 1503, 1519, 1524 cm^{-1};[19] liquid, 1517 cm^{-1})[46] and is comparable to that of [F_3S≡NXeF][AsF_6] (1527, 1542, 1548 cm^{-1});[19] however, a larger complexation shift [43 cm^{-1}] is calculated for the gas-phase species. The average out-of-phase and in-phase $\nu(SF_3)$ frequencies increase by 66 [95] cm^{-1} and 43 [78] cm^{-1}, respectively, upon complexation, and the average in-phase and out-of-phase bending frequencies shift to higher frequency by 16, 5, and 4 [24, 18, 10] cm^{-1}, which are less than or similar to the complexation shifts observed for [F_3S≡NXeF][AsF_6].[19] These high-frequency shifts are in accord with the N≡S and S−F bond length contractions that result from adduct formation with the F_4S=NXe^+ cation (see X-ray Crystallography). Complexation shifts for F_4S=N−Xe---N≡SF_3^+ are less than those of F_3S≡$NXeF^+$ because F_4S=N−Xe^+ is a weaker Lewis acid than XeF^+ (see calculated donor-acceptor adduct dissociation energies, Computational Results) and are in accordance with the longer Xe---N distance in F_4S=N−Xe---N≡SF_3^+ (2.583(3) Å) than in F_3S≡$NXeF^+$ (2.236(4) Å).

(b) [$F_3S(N≡SF_3)_2$][AsF_6]. The Raman spectrum of [$F_3S(N≡SF_3)_2$][AsF_6] (Figure 4) was assigned by comparison with those of SF_3^+ in its AsF_6^-,[23,39] SbF_6^-,[23] PF_6^-,[23,39] and BF_4^-,[23,37,39] salts and by comparison with free N≡SF_3,[19] adducted N≡SF_3 in [F_3S≡NXeF][AsF_6],[19] and F_4S=N−Xe---N≡SF_3^+ (vide supra) as well as by comparison with the calculated frequencies derived for the gas-phase energy-minimized geometry of the [$F_3S(N≡SF_3)_2$][AsF_6] ion pair (see Table 5, Computational Results). The vibrational modes of AsF_6^- in the ion pair were assigned by comparison with those of [F_4S=NXe][AsF_6],[11] [$F_5SN(H)Xe$][AsF_6],[27] [$F_5TeN(H)Xe$][AsF_6],[26] [F_5TeOXe][AsF_6],[47] [XeF][AsF_6],[48] and [KrF][AsF_6].[49] Calculated frequencies for the PBE1PBE/aug-ccpVTZ-(-PP) level of theory, the highest level of theory available for the ion pair in this work, appear in square brackets in the following discussion.

The 57 vibrational modes of the [$F_3S(N≡SF_3)_2$][AsF_6] ion pair under C_1 symmetry (see Computational Results) belong to A irreducible representations, which are both Raman- and infrared-active. The cation-anion fluorine bridge interaction lowers the O_h symmetry of the anion (see X-ray Crystal Structures of [F_4S=N−Xe---N≡SF_3]-[AsF_6] and [$F_3S(N≡SF_3)_2$][AsF_6]), and additional lines in the vibrational spectrum were consequently observed. The vibrational bands of the anion were also assigned under C_1 symmetry of the ion pair. A total of 17 vibrational bands were observed that are derived from their counterparts under O_h symmetry. The anion assignments are correlated to the irreducible representations $A_{1g}+E_g+2T_{1u}+T_{2g}+T_{2u}$ under O_h symmetry, with only three bands being further split by symmetry-lowering of the anion [E_g and one T_{1u}], for a total of 17 observed bands (correlations with O_h symmetry are given in square brackets), namely, 690, 702, 710, and 719 [T_{1u}]; 677 [A_{1g}]; 504, 580, and 586 [E_g]; 396, 400, and 406 [T_{1u}]; 372, 381, and 387 [T_{2g}]; and 278, 285, and 294 [T_{2u}] cm^{-1}. A factor-group analysis correlating the ion-pair symmetry (C_1) to the crystal site symmetry (C_1) and to the unit cell symmetry (C_{2h}) is provided in Table S3 and is discussed in the Supporting Information.

The calculated vibrational frequencies for [$F_3S(N≡SF_3)_2$][AsF_6] are in good agreement with the experimental frequencies. The ν(S−F) stretches of SF_3^+ at 859, 873 [843, 862], 899 [883], 919, and 922 [903] cm^{-1} occur at lower frequencies than the ν(S−F) stretches of the BF_4^- (911, 914, 937 cm^{-1}),[39] AsF_6^- (926, 945, 960 cm^{-1}),[39] and PF_6^- (929, 954, 964 cm^{-1})[39] salts, but the δ(F−S−F) bends at 396 [379], 406 [395], 412 [402], 529, 531 [517], 536 [518], 557, and 564 [527] cm^{-1} are in better agreement with those of the BF_4^- (409, 526 cm^{-1}),[39] AsF_6^- (411, 530 cm^{-1}),[39] and PF_6^- (408, 531 cm^{-1})[39] salts. The intense high-frequency bands at 1535 [1569] and 1546 [1574] cm^{-1} are assigned to the coupled ν(N1≡S1) − ν(N2≡S2) and ν(N1≡S1) + ν(N2≡S2) stretches, respectively, and are consistent with the two adducted N≡SF_3 molecules of the $F_3S(N≡SF_3)_2^+$ cation. The ν(N≡S) stretching bands of the adducted N≡SF_3 molecules occur at higher frequencies relative to those of N≡SF_3 [1503] (liquid, 1517;[46] solid, 1503, 1519, 1524 cm^{-1}[19]) and are in close agreement with those of F_3S≡$NXeF^+$ (1527, 1542, 1548 cm^{-1})[19] and F_4S=N−Xe---N≡SF_3^+ (1543, 1548 cm^{-1}) (vide supra). The average out-of-phase and in-phase $\nu(SF_3)$ frequencies, all of which are coupled for the two adducted N≡SF_3 molecules, increase by 55 (liquid) and 42 (solid) [47] cm^{-1} and by 34 (liquid) and 28 (solid) [48] cm^{-1}, respectively, upon complexation. The average in-phase and out-of-phase N≡SF_3-group bending frequencies, all of which are coupled as above, exhibit complexation shifts that are less than or equal to those observed in F_3S≡$NXeF^+$ [19] and F_4S=N−Xe---N≡SF_3^+ (vide supra). These high-frequency shifts are in accord with the N≡S and S−F bond length contractions that result from adduct formation with the SF_3^+ cation (see X-ray Crystallography and Computational Results).

Computational Results. Quantum-chemical calculations were carried out at the MP2, B3LYP, and PBE1PBE levels for F_4S=N−Xe---N≡SF_3^+ and at the B3LYP and PBE1PBE levels only for the ion pair, [$F_3S(N≡SF_3)_2$]-[AsF_6], due to computational constraints. All levels employed aug-cc-pVTZ(-PP) basis sets. The calculations were used to aid in the vibrational assignments (see Raman Spectroscopy) and to gain insight into the structure and bonding of this cation. Comparisons of the calculated and experimental geometrical parameters and vibrational frequencies with those of the benchmarks, [F_4S=NXe]-[AsF_6][11] and F_4S=NF,[11,28] showed that the MP2 calculations provided the best overall agreement. Therefore, the vibrational assignments for F_4S=N−Xe---N≡SF_3^+ are based on the MP2 results (Table 4), which are reported in square brackets in the ensuing discussion. For [$F_3S(N≡SF_3)_2$][AsF_6], the PBE1PBE level provided better overall agreement with the experimental geometry and vibrational frequencies (Table 5). The PBE1PBE values referred to in the ensuing discussion of the ion pair appear in parentheses.

(46) This work.
(47) Fir, B. A.; Mercier, H. P. A.; Sanders, J. C. P.; Dixon, D. A.; Schrobilgen, G. J. *J. Fluorine Chem.* **2001**, *110*, 89–107.
(48) Gillespie, R. J.; Landa, B. *Inorg. Chem.* **1973**, *12*, 1383–1388.
(49) Gillespie, R. J.; Schrobilgen, G. J. *Inorg. Chem.* **1976**, *15*, 22–31.

Table 5. Experimental Raman Frequencies and Intensities, and Calculated Vibrational Frequencies, Intensities, and Assignments for the $[F_3S(N{\equiv}SF_3)_2][AsF_6]$ Ion Pair

freq, cm^{-1}			assgnts[c]	
	calcd[b]			
exptl[a]	PBE1PBE	B3LYP	$[F_3S(N{\equiv}SF_3)_2][AsF_6]$ (C_1)	AsF_6^- (O_h)
1546 (63)	1574 (95) [198]	1535 (98) [182]	ν(N1S1 + N2S2)	
1535 (68)	1569 (37) [290]	1530 (40) [255]	ν(N1S1 – N2S2)	
922 (70) 919 (31)	903 (100) [236]	872 (109) [209]	ν(S3F8 + S3F9)	
899 (72)	883 (22) [350]	851 (25) [298]	ν(S3F8 – S3F9)	
888 (46)	871 (6) [159]	822 (6) [178]	ν(S1F2 – S1F3) + ν(S2F6 – S2F4)	
881 sh	865 (3) [50]	816 (2) [101]	ν(S1F2 – S1F3) + ν(S2F4 – S2F6)	
873 (6)	862 (9) [509]	819 (12) [469]	ν(S3F7)	
864 (15)	845 (9) [15]	797 (9) [13]	ν(S1F2 + S1F3) – ν(S1F1) + ν(S2F4 + S2F6) – ν(S2F5)	
859 (23)	843 (8) [88]	796 (7) [135]	ν(S1F2 + S1F3) – ν(S1F1) – ν(S2F4 + S2F6) + ν(S2F5) + ν(S3F7)	
815 (45) 809 (100)	810 (50) [105]	767 (53) [109]	ν(N1S1) + ν($S1F_3$) + ν(N2S2) + ν($S2F_3$)	
798 (3)	804 (3) [289]	761 (3) [278]	ν(N1S1) + ν($S1F_3$) – ν(N2S2) – ν($S2F_3$)	
719 (4)	742 (2) [171]	716 (2) [167]	ν(As1F11 – As1F14)	[ν_3 (T_{1u})]
710 (13)	724 (4) [119]	700 (3) [122]	ν(As1F13)	
702 (20)	722 (1) [153]	698 (1) [151]	ν(As1F12 – As1F15)	
690 (4)				
677 (88)	665 (15) [60]	641 (17) [52]	ν(As1F11 + As1F14) + ν(As1F12 + As1F15)	[ν_1 (A_{1g})]
586 (16) 580 (5)	584 (1) [2]	567 (1) [2]	ν(As1F11 + As1F14) – ν(As1F12 + As1F15)	[ν_2 (E_g)]
564 (10) 557 (2)	527 (1) [31]	512 (1) [31]	δ(S3F7F8F9) o.o.p.	
536 (15)	518 (1) [24]	500 (1) [21]	δ(S1F1F2F3) o.o.p. + δ(S2F4F5F6) o.o.p.	
531 (9) 529 (6)	517 (2) [15]	500 (2) [14]	δ(S1F1F2F3) o.o.p. – δ(S2F4F5F6) o.o.p.	
504 (1) br	487 (2) [62]	460 (2) [52]	ν(As1F10)	
462 (22)	443 (2) [29]	422 (2) [26]	δ(N1S1F2F3) o.o.p. + δ(N2S2F5F6) o.o.p.	
454 (34)	443 (6) [5]	422 (7) [4]	δ(N1S1F2F3) o.o.p. – δ(N2S2F5F6) o.o.p.	
446 (33)	438 (6) [10]	418 (6) [8]	δ(N1S1F1F3) o.o.p. + δ(N2S2F4F5) o.o.p.	
424 (3)	437 (<1) [19]	417 (<1) [15]	δ(N1S1F1F3) o.o.p. – δ(N2S2F4F5) o.o.p.	
420 (3)	419 (<1) [54]	409 (<1) [48]	ν(S3---F10)	
412 (5)	402 (<1) [23]	388 (<1) [19]	δ(F7S3F8) – δ(F7S3F9)	
406 (3)	395 (<1) [28]	383 (<1) [42]	δ(As1F10F12F13F15) o.o.p.[d] – δ(F8S3F9)	[ν_4 (T_{1u})]
400 (3)	392 (<1) [52]	382 (<1) [52]	δ(As1F10F11F13F14) o.o.p.[e]	
396 (3)	379 (1) [108]	362 (1) [78]	δ(As1F11F12F14F15) o.o.p.[f] + δ(F8S3F9)	
387 (8)	371 (1) [2]	362 (1) [2]	δ(F12As1F14) + δ(F13As1F15)	
381 (8)	359 (1) [39]	346 (1) [76]	δ(F10As1F11) + δ(F13As1F14)	
372 sh	349 (<1) [<1]	338 (<1) [<1]	δ(F12As1F13) + δ(F10As1F15) + δ(N1S1F3) + δ(F1S1F2) + δ(N2S2F4) + δ(F5S2F6)	[ν_5 (T_{2g})]
370 (44)	348 (4) [11]	335 (5) [14]	δ(N1S1F1) + δ(F2S1F3) + δ(N2S2F5) + δ(F6S2F7)	
365 (22)	348 (1) [2]	335 (<1) [2]	δ(F10As1F12) + δ(F13As1F15) + δ(N1S1F1) + δ(F2S1F3) + δ(N2S2F5) + δ(F4S2F6)	
361 (19)	343 (<1) [1]	330 (<1) [1]	δ(N1S1F2) + δ(F1S1F3) – δ(N2S2F6) – δ(F4S2F5)	
354 (53)	343 (4) [<1]	330 (4) [<1]	δ(N1S1F2) + δ(F1S1F3) + δ(N2S2F6) + δ(F4S2F5)	
294 (7)	256 (<1) [21]	251 (<1) [26]	δ(F10As1F13) – δ(F12As1F15) o.o.p.[d]	[ν_6 (T_{2u})]
285 (3)	243 (<1) [1]	237 (<1) [1]	δ(F10As1F13) – δ(F11As1F14) o.o.p.[e]	
278 (2) br	224 (<1) [<1]	216 (<1) [<1]	δ(F11As1F14) – δ(F12As1F15) o.o.p.[f]	
187 sh	193 (<1) [11]	181 (<1) [7]	ρ_t(F8S3F9)	
	191 (<1) [6]	181 (<1) [11]	ρ_w(F8S3F9) + ρ_r(F7S3F8)	
n.o.	145 (<1) [<1]	132 (<1) [<1]	SF_3^+ torsion about its own C_3-axis	
132 (6)	137 (1) [24]	135 (1) [23]	ν(N1S3 + N2S3)	
n.o.	95 (<1) [<1]	86 (<1) [<1]	δ(S1N1S3) o.o.p. + δ(S2N2S3) o.o.p.	
119 (6)	90 (1) [10]	84 (1) [8]	δ(S1N1S3) i.p. + δ(S2N2S3) i.p.	
112 (8)	87 (1) [7]	82 (1) [7]	δ(S1N1S3) i.p. – δ(S2N2S3) i.p.	
n.o.	77 (<1) [1]	69 (<1) [<1]	δ(S3F10As1) i.p.	
101 (7)	72 (1) [9]	66 (1) [7]	ν(N1S3 – N2S3)	
n.o.	58 (<1) [4]	50 (<1) [3]	coupled deformation mode	
n.o.	50 (<1) [<1]	45 (<1) [<1]	δ(N1S3N2) i.p.	
n.o.	49 (<1) [<1]	41 (<1) [<1]	coupled deformation mode	
n.o.	43 (<1) [2]	39 (<1) [2]	δ(N1S3N2) o.o.p.	
n.o.	41 (<1) [<1]	33 (<1) [<1]	$N{\equiv}SF_3$ torsions about N≡S bond	
n.o.	37 (<1) [<1]	32 (<1) [<1]	coupled deformation modes	
n.o.	32 (<1) [<1]	29 (<1) [<1]		
n.o.	18 (<1) [1]	15 (<1) [1]		
n.o.	12 (<1) [<1]	15 (<1) [<1]	δ(S3F10As1) o.o.p.	

[a] Values in parentheses denote experimental Raman intensities; abbreviations denote shoulder (sh), broad (br), and not observed (n.o.). [b] The aug-cc-pVTZ basis set. Calculated Raman intensities (in $Å^4$ amu^{-1}) are given in parentheses; calculated infrared intensities (in km mol^{-1}) are given in brackets. Bands corresponding to residual *cis*-N_2F_2 appear at 354*, 729*, 888*, 946 (5), and 1519† cm^{-1}, where * denotes coincidence with $F_3S(N{\equiv}SF_3)_2^+$ bands and † denotes coincidence with ν(S≡N) of unreacted $F_4S{=}N{-}Xe{---}N{\equiv}SF_3^+$. [c] Abbreviations denote twist (ρ_t), wag (ρ_w), rock (ρ_r), out-of-plane (o.o.p.), and in-plane (i.p.), where the planes are defined by the atoms they contain, unless otherwise specified. [d] Plane defined by As1, F10, F12, F13, and F15. [e] Plane defined by As1, F10, F11, F13, and F14. [f] Plane defined by As1, F11, F12, F14, and F15.

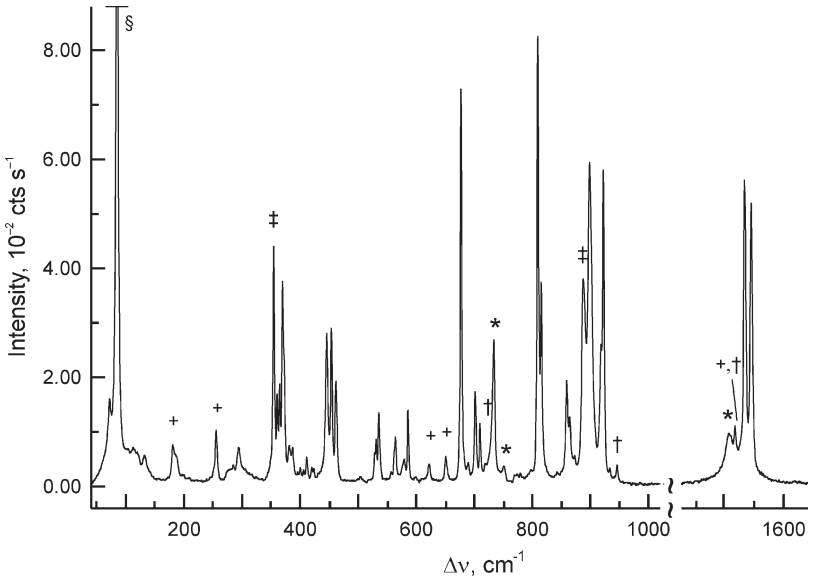

Figure 4. The Raman spectrum of $[F_3S(N{\equiv}SF_3)_2][AsF_6]$ recorded at −160 °C using 1064-nm excitation. Symbols denote bands from unreacted $[F_4S{=}N{-}Xe{-}{-}{-}N{\equiv}SF_3][AsF_6]$ (+), *cis*-N_2F_2 (†), coincidence of $F_3S(N{\equiv}SF_3)_2^+$ and *cis*-N_2F_2 bands (‡), FEP sample tube lines (*), and an instrumental artifact (§).

(a) Calculated Geometries. (i) $F_4S{=}N{-}Xe{-}{-}{-}N{\equiv}SF_3^+$. Although close to C_s symmetry, the MP2, PBE1PBE, and B3LYP energy-minimized structures of $F_4S{=}N{-}Xe{-}{-}{-}N{\equiv}SF_3^+$ optimized to C_1 symmetry with all vibrational frequencies real. These calculations well-reproduced the experimental geometric parameters of the coordinated $F_4S{=}NXe^+$ cation, with the largest discrepancies occurring for the Xe---N≡S interaction in the adduct cation. The calculated Xe---N [2.524 Å] and N≡S [1.428 Å] bond lengths are in very good agreement with the experimental values (2.583(3) and 1.398(3) Å). The calculated Xe---N≡S angle was less distorted from linearity [178.6°] than the experimental angle, 148.0(2)°, which is undoubtedly influenced by crystal packing (see X-ray Crystal Structures of $[F_4S{=}N{-}Xe{-}{-}{-}N{\equiv}SF_3][AsF_6]$ and $[F_3S(N{\equiv}SF_3)_2][AsF_6]$). The energy difference between the bent and near-linear geometries is small [7.4 kJ mol^{-1}], as is the case for the $F_3S{\equiv}NXeF^+$ cation [7.9 kJ mol^{-1}],[19] showing the Xe---N≡S angle to be very deformable. The torsional angle defined by N1, Xe, N2, and S2 is substantially different in the experimental (−117.0(3)°) and calculated [−30.1°] geometries. The torsional angle is also very deformable (the calculated torsional frequency is 2 cm^{-1}), and again the difference is most likely a consequence of crystal packing.

(ii) $[F_3S(N{\equiv}SF_3)_2][AsF_6]$. The SF_3^+ cation of the energy-minimized structure of $[F_3S(N{\equiv}SF_3)_2][AsF_6]$ optimized to C_1 symmetry at the B3LYP and PBE1PBE levels using the aug-cc-pVTZ(-PP) basis sets and was very near C_s symmetry. While the gross features of the cation, bridging anion, and adducted N≡SF_3 molecules were well-reproduced, the S−F, S≡N, and bridging As−F bonds were overestimated, and the S---F and S---N contacts were underestimated, with the S---F−As bridge bonds showing the greatest discrepancy. In the energy-minimized gas-phase SF_3^+ cation (C_{3v} symmetry), the S−F bond length [1.514 Å] is the same, within $\pm 3\sigma$, as that observed for $[F_3S(N{\equiv}SF_3)_2][AsF_6]$ (av., 1.517(2) Å), but the calculated F−S−F bond angles [99.5°] are greater than in the experimental structure (av., 96.4(2)°), which may result from steric effects of the adducted N≡SF_3 molecules and coordinated AsF_6^- anion of the ion pair.

(b) Effect of Adduct Formation on the Geometry of N≡SF_3. Upon coordination of N≡SF_3, the valence electron lone pair on the nitrogen atom changes from predominantly s character to sp hybrid character, leading to strengthening and contraction of the S−N σ bond.[15] This also removes charge density from the S atom and results in more covalent and shorter S−F bonds. This bonding model is in accordance with the trend in the calculated bond lengths for free N≡SF_3,[19] and adducted N≡SF_3 in $F_4S{=}N{-}Xe{-}{-}{-}N{\equiv}SF_3^+$ and $[F_3S(N{\equiv}SF_3)_2][AsF_6]$, where the S≡N bonds shorten by 0.017 and 0.023/0.023 Å, respectively, and the S−F bonds (average) shorten by 0.029 and 0.073/0.056 Å, respectively. The calculated trends agree with the experimental trends; that is, upon adduct formation, the S≡N bonds shorten by 0.017(4) and 0.031(4)/0.023(4) Å, respectively, and the S−F bonds (average) shorten by 0.026(3) and 0.031(3)/0.028(3) Å, respectively. This trend is also observed for $F_3S{\equiv}NXeF^+$, where the experimental S≡N and S−F (average) bonds shorten by 0.018(4) and 0.049(4) Å,[19] and the calculated bond lengths shorten by 0.019 and 0.047 Å.[46] The increased degree of sp mixing that is postulated to occur upon coordination not only results in S−N bond shortening but apparently also influences the degree of sp^3 hybridization at the sulfur, with decreasing p character leading to somewhat greater s character and somewhat more open F−S−F angles. The latter increase by 3.2(3)° ($F_3S{\equiv}NXeF^+$),[19] 1.2(3)° ($F_4S{=}NXe{-}{-}{-}N{\equiv}SF_3^+$),[46] 0.9(2) and 1.1(2)° ($F_3S(N{\equiv}SF_3)_2^+$),[46] and 1.8(3)° ($CpFe(CO)_2N{\equiv}SF_3)^+$,[18] relative to N≡$SF_3$.[34]

(c) NBO Charges, Valencies, and Bond Orders. The NBO charges, valencies, and bond orders calculated using MP2, PBE1PBE, and B3LYP methods for $F_4S{=}N{-}Xe{-}{-}{-}N{\equiv}SF_3^+$ are listed in Table S4. The $F_4S{=}N{-}Xe{-}{-}{-}N{\equiv}SF_3^+$ cation is compared with $F_4S{=}NXe^+$,[11] $F_3S{\equiv}NXeF^+$, and $F_5SN(H)Xe^+$,[27] and

adducted $N{\equiv}SF_3$ is compared with $N{\equiv}SF_3$ and $F_3S{\equiv}NXeF^+$ (Table S5). The observed and calculated geometrical changes that occur upon coordination of $N{\equiv}SF_3$ are reflected in the natural bond orbital (NBO) analyses. Only the MP2 values are referred to in the ensuing discussion, and these are summarized in Scheme 2.

Scheme 2. Natural Bond Orbital (NBO) Charges, Valencies, and Bond Orders for Selected Atoms and Bonds in $N{\equiv}SF_3$, XeF^+, $F_3S{\equiv}NXeF^+$, $F_4S{=}NXe^+$, and $F_4S{=}N{-}Xe{-}{-}{-}N{\equiv}SF_3^+$ Calculated at the MP2/aug-cc-pVTZ(-PP) Level of Theory

Charges

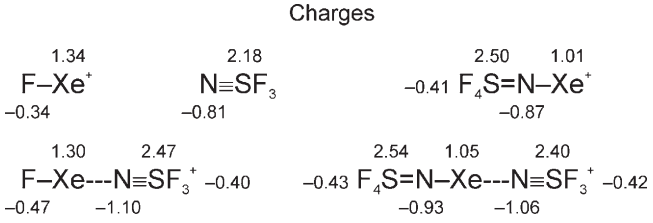

Valencies

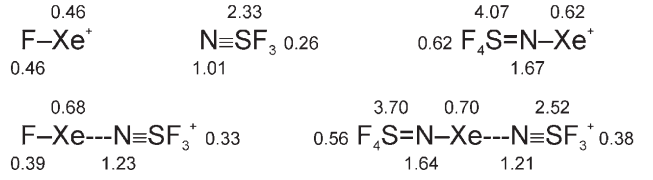

Bond Orders

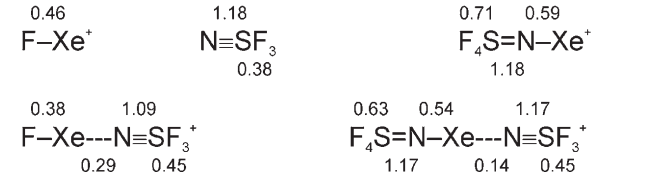

(i) $F_4S{=}N{-}Xe{-}{-}{-}N{\equiv}SF_3^+$. The NBO parameters for $F_4S{=}NXe^+$ do not exhibit large changes upon $N{\equiv}SF_3$ coordination. The positive charges of $F_4S{=}N{-}Xe{-}{-}{-}N{\equiv}SF_3^+$ reside on xenon and both sulfur atoms, with the charges on S1 [2.51] and the fluorines bonded to S1 [av., −0.43] remaining essentially unchanged with respect to those of $F_4S{=}NXe^+$ [2.50; av., −0.41]. Comparison of XeF^+ with $F_3S{\equiv}NXeF^+$ also shows little change in xenon charge upon coordination. Upon coordination of $N{\equiv}SF_3$, the absolute charges on Xe and N of $F_4S{=}NXe^+$ increase somewhat when compared with those of free $F_4S{=}NXe^+$. This is consistent with a more polar Xe−N bond in $F_4S{=}N{-}Xe{-}{-}{-}N{\equiv}SF_3^+$, which is corroborated by the somewhat lower Xe−N bond order of the adduct [0.54] when compared with that of $F_4S{=}NXe^+$ [0.59]. Both bond orders are, however, similar to that of $F_5SN(H)Xe^+$ [0.60], which are nearly double that of $F_3S{\equiv}NXeF^+$ [0.29] and are indicative of much stronger covalent bonding between xenon and nitrogen in $F_4S{=}NXe^+$, $F_4S{=}N{-}Xe{-}{-}{-}N{\equiv}SF_3^+$, and $F_5SN(H)Xe^+$. The lower S1 [3.70] and F-on-S1 [av., 0.56] valencies compared with those of the free cation [4.07; av., 0.62] are more consistent with the lower S1−F bond orders in $F_4S{=}N{-}Xe{-}{-}{-}N{\equiv}SF_3^+$ [0.63] than in $F_4S{=}NXe^+$ [0.71]. The total NBO bond orders of the linear N---Xe−F and N−Xe---N moieties of $F_3S{\equiv}N{-}Xe{-}F^+$ and $F_4S{=}N{-}Xe{-}{-}{-}N{\equiv}SF_3^+$ are nearly equal [0.67 and 0.68], but the Xe−F and Xe−N bond orders of their Lewis acid precursors, XeF^+ [0.46] and $F_4S{=}NXe^+$ [0.59], show that the Xe−N bond of $F_4S{=}NXe^+$ is more covalent.

The NBO parameters of coordinated $N{\equiv}SF_3$ display the most pronounced changes upon coordination to $F_4S{=}NXe^+$ and XeF^+, corroborating the experimental and calculated S−N and S−F bond length contractions. The increase in the valency of N upon adduct formation with $F_4S{=}NXe^+$ [0.20] is significantly greater than that of Xe [0.08], whereas the increases are equal for $F_3S{\equiv}NXeF^+$ [N, 0.22; Xe, 0.22]. The modest valency increase for Xe is corroborated by the low Xe---N bond order [0.14], which is half that of $F_3S{\equiv}NXeF^+$ [0.29]. Contraction of the S≡N and S−F bonds in $F_4S{=}N{-}Xe{-}{-}{-}N{\equiv}SF_3^+$ is in accord with increased N, S, and F valencies and increased S−F bond orders. The negative charge drift to the N donor atom that occurs for $F_4S{=}N{-}Xe{-}{-}{-}N{\equiv}SF_3^+$ and $F_3S{\equiv}NXeF^+$ upon $N{\equiv}SF_3$ coordination is essentially matched by the increased positive charges on the S atoms of their $N{\equiv}SF_3$ donor molecules, leaving the Xe charges essentially unchanged. Thus, the Xe---N donor-acceptor bonds in these adduct cations are essentially polar interactions, which induce rehybridization of their nitrogen donor atom lone pairs upon adduct formation, providing the lone pairs and the N−S σ bonds with enhanced sp characters. Although this results in shorter N−S bonds and greater N and S valencies for the adducted $N{\equiv}SF_3$ molecules, their total N−S bond orders remain essentially unchanged. No significant change in the S≡N bond order occurs upon adduct formation with $F_4S{=}NXe^+$, and a bond order decrease of only 0.09 occurs upon $F_3S{\equiv}NXeF^+$ formation with the stronger Lewis acid, XeF^+ (vide infra).

(ii) $[F_3S(N{\equiv}SF_3)_2][AsF_6]$. Only the adducted $N{\equiv}SF_3$ molecules in $F_3S{\equiv}NXeF^+$, $F_4S{=}N{-}Xe{-}{-}{-}N{\equiv}SF_3^+$, and the $[F_3S(N{\equiv}SF_3)_2][AsF_6]$ ion pair are compared. The PBE1PBE/aug-cc-pVTZ(-PP) results (Table S6) are referred to in the ensuing discussion because they represent the highest level of theory available for the $[F_3S(N{\equiv}SF_3)_2][AsF_6]$ ion pair in the present study. As in the cases of $F_3S{\equiv}NXeF^+$ and $F_4S{=}N{-}Xe{-}{-}{-}N{\equiv}SF_3^+$, the experimental and calculated bond length contractions of the S−N and S−F bonds of coordinated $N{\equiv}SF_3$ are corroborated by the NBO analyses (Table S5). Negative charge drifts to the N donor atoms (−0.79 to −0.99) occur upon $N{\equiv}SF_3$ coordination that are matched by the increased positive charges on the S atoms (2.13−2.33) of the donor $N{\equiv}SF_3$ molecules. The induced change in S−N bond polarization is similar to that in the XeF^+ and $F_4S{=}N{-}Xe^+$ adducts. The valency increases for N1 and N2 in $[F_3S(N{\equiv}SF_3)_2][AsF_6]$ that occur upon adduct formation (0.56) are, however, substantially greater than for $F_4S{=}N{-}Xe{-}{-}{-}N{\equiv}SF_3^+$ (0.16) and $F_3S{\equiv}NXeF^+$ (0.15). The Xe---N donor-acceptor bond orders are significantly greater than the S---N donor-acceptor bond orders (0.09) of the SF_3^+ adduct, but the S1−N1/S2−N2 bond orders increase by 0.44, which is substantially greater than for the xenon adducts calculated at the PBE1PBE level (cf. Scheme 2 and Tables S4 and S5). The greater experimental S−N and S−F bond length contractions

observed for the adducted $N{\equiv}SF_3$ molecules in $F_3S(N{\equiv}SF_3)_2^+$ are also accompanied by significantly greater valency increases for S1 and S2 (1.15) and for F bonded to S1 and S2 (0.29), and by larger increases in the S1−F/S2−F bond orders (0.36). Despite the formation of a more weakly covalent donor-acceptor bond and the similar S−N bond polarizations induced by the SF_3^+ cation, the latter cation apparently has more pronounced effects on the extent of sp hybridization of the S−N σ bond and associated NBO parameters than do the XeF^+ and $F_4S{=}NXe^+$ cations.

(d) Nature of the Xenon(II)-Nitrogen Adduct Bond. The gas-phase donor-acceptor dissociation energies for $F_4S{=}N{-}Xe{---}N{\equiv}SF_3^+$, $F_3S{\equiv}NXeF^+$, $F_3S{\equiv}NAsF_5$, and the related $HC{\equiv}NXeF^+$ cation were calculated at the MP2 level of theory and are listed in Scheme 3. The $F_4S{=}N{-}Xe{---}N{\equiv}SF_3^+$ dissociation energy is considerably less than that of the more covalent $F_3S{\equiv}NXeF^+$ and $HC{\equiv}NXeF^+$ cations, but significantly greater than the dissociation energy of $F_3S{\equiv}NAsF_5$. The NBO Xe---N bond order of $F_4S{=}N{-}Xe{---}N{\equiv}SF_3^+$ [0.14] is only half that of $F_3S{\equiv}NXeF^+$ [0.29] (Tables S4 and S5), in accord with the calculated dissociation energies and the structural findings which show a significantly longer Xe---N bond for $F_4S{=}N{-}Xe{---}N{\equiv}SF_3^+$ (2.583(3) Å) than for $F_3S{\equiv}NXeF^+$ (2.236(4) Å)[19] and $HC{\equiv}NXeF^+$ (2.235(3)).[30]

As in the cases of $HC{\equiv}NNgF^+$ (Ng = Kr, Xe)[50] and $F_3S{\equiv}NXeF^+$,[19] the Xe---N bond of $F_4S{=}N{-}Xe{---}N{\equiv}SF_3^+$ may be regarded in terms of a mutual penetration of the outer diffuse nonbonded electron densities of Xe, a torus of three valence electron lone pairs,[51] and of the N electron lone pair. The torus of Xe valence density exposes the positive core charge of Xe, allowing the Xe atom to polarize the N donor atom. The highly polar nature of the interaction only produces a small shared density, as reflected in the low Xe---N bond orders and small changes in Xe and N valencies (Scheme 2 and Tables S4 and S5). Although the negative charge drift to the N donor atom is essentially matched by the increased positive charge on the S atom of the donor molecule, little charge is actually transferred to the Xe acceptor atom. The interaction is primarily electrostatic, and its strength is determined by the extent of interpenetration of the closed-shell densities of Xe and N, which leads to little modification of the Xe charge but significant polarization and negative charge increase on the N donor atom.

Scheme 3. Dissociation Energies (kJ mol^{-1}) for Selected Donor-Acceptor Adducts Calculated at the MP2/aug-cc-pVTZ(-PP) Level of Theory

$F_3S{\equiv}NAsF_5 \rightarrow F_3S{\equiv}N{:} + AsF_5$ 38.1

$F_4S{=}NXe{---}N{\equiv}SF_3^+ \rightarrow F_3S{\equiv}N{:} + F_4S{=}NXe^+$ 85.2

$F_3S{\equiv}NXeF^+ \rightarrow F_3S{\equiv}N{:} + XeF^+$ 173.2

$HC{\equiv}NXeF^+ \rightarrow HC{\equiv}N{:} + XeF^+$ 180.9

Conclusions

Both $F_4S{=}NXe^+$ and SF_3^+ have been shown to form Lewis acid-base adducts with $N{\equiv}SF_3$. The $[F_4S{=}N{-}Xe{---}N{\equiv}SF_3][AsF_6]$ salt has been synthesized by reaction of $[F_3S{\equiv}NXeF][AsF_6]$ with liquid $N{\equiv}SF_3$ solvent. The rearrangement is proposed to occur through an S_N2 mechanism involving fluoride ion displacement from the adducted XeF group of $F_3S{\equiv}NXeF^+$ by $N{\equiv}SF_3$, followed by fluoride ion coordination to sulfur. The resulting $F_4S{=}N{-}Xe{---}N{\equiv}SF_3^+$ cation provides a rare example of xenon bound to nitrogen of an imido group and among the shortest Xe−N bonds presently known, as well as the first example of an N−Xe−N linkage to be characterized by single-crystal X-ray diffraction. The reaction of $[F_4S{=}N{-}Xe{---}N{\equiv}SF_3][AsF_6]$ with $N{\equiv}SF_3$ resulted in the redox elimination of Xe and *cis*-N_2F_2 and formation of $[F_3S(N{\equiv}SF_3)_2][AsF_6]$, along with NF_3 as a minor byproduct. The latter salt is one of only a few main-group coordination compounds of $N{\equiv}SF_3$ to have been characterized by single-crystal X-ray diffraction, and the first definitively characterized example of the SF_3^+ cation coordinated to a ligand atom other than fluorine. The donor-acceptor interactions of both cations are highly polar in nature. The S≡N bonds of $F_4S{=}N{-}Xe{---}N{\equiv}SF_3^+$ and $F_3S(N{\equiv}SF_3)_2^+$ are shorter than that of the free $N{\equiv}SF_3$ molecule, in accord with the prevalent bonding description; that is, upon coordination, the nitrogen donor atom and its valence electron lone pair are polarized by the positive xenon Lewis acid center, inducing lone pair rehybridization from predominantly s character to sp character, leading to strengthening and contraction of the S−N σ bond of the $N{\equiv}SF_3$ ligand molecule.

Experimental Section

Apparatus and Materials. All manipulations involving air-sensitive materials were carried out under anhydrous conditions, as previously described.[52] Volatile materials were handled on vacuum lines constructed of nickel, stainless steel, and FEP. Nonvolatile materials were handled in a drybox. Reaction vessels and Raman sample tubes (¼-in. o.d.) and NMR sample tubes (4-mm o.d.) were fabricated from FEP tubing that had been heat-sealed on one end and heat-flared to a 45° angle on the other end for connection to Kel-F valves by means of compression fittings. All FEP reaction vessels and sample tubes were rigorously dried under dynamic vacuum prior to passivation with 1 atm of F_2 gas. Literature methods were used to prepare $N{\equiv}SF_3$[53] and $[F_3S{\equiv}NXeF][AsF_6]$.[19] Specific procedures relating to the syntheses and growth of $[F_4S{=}N{-}Xe{---}N{\equiv}SF_3][AsF_6]$ and $[F_3S(N{\equiv}SF_3)_2][AsF_6]$ crystals suitable for structure determination by single-crystal X-ray diffraction are found in the Crystal Growth section.

Synthesis of $[F_4S{=}N{-}Xe{---}N{\equiv}SF_3][AsF_6]$. In a typical synthesis, $[F_3S{\equiv}NXeF][AsF_6]$ (0.1309 g, 0.2959 mmol) was prepared[17] in a ¼-in. o.d. FEP reaction tube fitted with a Kel-F valve. The reactor was connected to an FEP submanifold that was, in turn, connected to a stainless steel cylinder containing $N{\equiv}SF_3$. The cylinder was fitted with two 316 stainless steel Whitey (SS-ORM2) valves separated by a ca. 5-cm length of ¼-in. o.d. stainless steel tubing that afforded a volume (ca. 1.4 mL) which was pressurized to the autogenous pressure of $N{\equiv}SF_3$ at room temperature. Successive 1.4 mL aliquots of gaseous $N{\equiv}SF_3$ were metered into the reaction vessel by condensation

(50) MacDougall, P. J.; Schrobilgen, G. J.; Bader, R. F. W. *Inorg. Chem.* **1989**, *28*, 763–769.
(51) Mercier, H. P. A.; Moran, M. D.; Sanders, J. C. P.; Schrobilgen, G. J.; Suontamo, R. J. *Inorg. Chem.* **2005**, *44*, 49–60.
(52) Casteel, W. J., Jr.; Dixon, D. A.; Mercier, H. P. A.; Schrobilgen, G. J. *Inorg. Chem.* **1996**, *35*, 4310–4322.
(53) Mews, R.; Keller, K.; Glemser, O. *Inorg. Synth.* **1986**, *24*, 12–17.

at −196 °C to give a total of ca. 0.18 g (1.7 mmol) of $N{\equiv}SF_3$. The reaction vessel was initially warmed to −78 °C, followed by warming to −20 °C for ca. 6 h with occasional mixing. The white solid corresponding to $[F_3S{\equiv}NXeF][AsF_6]$ slowly dissolved in excess liquid $N{\equiv}SF_3$ to form a yellow solution from which a deep yellow microcrystalline solid deposited. With gradual warming to 0 °C over an additional 15 h period, the solid redissolved, and two liquid phases separated, a colorless upper layer and a deep yellow lower layer. Excess $N{\equiv}SF_3$ was removed under dynamic vacuum at −50 °C over a period of ca. 30 min, yielding a bright yellow powder, $[F_4S{=}N{-}Xe{---}N{\equiv}SF_3][AsF_6]$ (eq 1), which was stored at −78 °C until it was characterized by Raman spectroscopy.

Synthesis of $[F_3S(N{\equiv}SF_3)_2][AsF_6]$. In a typical synthesis, $[F_4S{=}N{-}Xe{---}N{\equiv}SF_3][AsF_6]$ (0.1456 g, 0.2669 mmol) was prepared in a ¼-in. o.d. FEP reaction tube fitted with a Kel-F valve following the procedure described above up to the point of solvent removal. At that point, the solution was maintained in liquid $N{\equiv}SF_3$ at 0 °C for an additional 6 h, over which time the solution slowly changed from yellow to colorless. Excess $N{\equiv}SF_3$ was then removed under dynamic vacuum at −50 °C over a period of ca. 5 min, yielding a friable white solid that was a mixture of $[F_3S(N{\equiv}SF_3)_2][AsF_6]$ and *cis*-N_2F_2 (eq 2), which was stored at −78 °C until it was characterized by Raman spectroscopy. Further pumping at −45 °C for ca. 15 min, resulted in removal of *cis*-N_2F_2 and coordinated $N{\equiv}SF_3$, yielding $[SF_3][AsF_6]$.

Crystal Growth of $[F_4S{=}N{-}Xe{---}N{\equiv}SF_3][AsF_6]$ and $[F_3S(N{\equiv}SF_3)_2][AsF_6]$. Thiazyl trifluoride ($N{\equiv}SF_3$, ca. 1 mL) was condensed onto $[F_3S{\equiv}NXeF][AsF_6]$ (0.1186 g, 0.2681 mmol) at −196 °C that had been synthesized in situ in one arm of a ¼-in. o.d. FEP T-shaped reactor fitted with a Kel-F valve. The reactor was warmed to −78 °C and pressurized to 1 atm with dry nitrogen before warming to −20 °C, and then to 0 °C, as described under the syntheses of these compounds (vide supra). While maintaining the solution temperature at 0 °C, the reaction vessel was attached to a vacuum line, and the arm containing the solution was inclined at ca. 5° from horizontal inside the glass Dewar of a crystal growing apparatus[54] that had been previously adjusted to 0 °C. The temperature was lowered over a period of 1 h to −10 °C, where it was held for a further 30 min to allow for more complete crystallization. The resulting crystalline material was isolated by decanting the solvent under dry nitrogen into the side arm of the FEP vessel, which was immersed in liquid nitrogen. This was followed by lowering the sample temperature to −40 °C and evacuation to remove residual $N{\equiv}SF_3$ followed by heat sealing off the side arm containing the supernatant at −196 °C. The crystalline sample was further dried under a dynamic vacuum at −80 °C before the crystallization vessel was backfilled with dry nitrogen and stored at −78 °C until suitable crystals could be mounted for X-ray structure determinations. A pale yellow, block-shaped crystal of $[F_4S{=}N{-}Xe{---}N{\equiv}SF_3][AsF_6]$, having the dimensions 0.22 × 0.20 × 0.16 mm^3, and a colorless, blade-shaped crystal of $[F_3S(N{\equiv}SF_3)_2][AsF_6]$, having the dimensions 0.28 × 0.12 × 0.06 mm^3, were selected at −104 ±2 °C and mounted in a cold stream (−173 °C) on the goniometer head of the X-ray diffractometer, as previously described.[55]

X-ray Crystallography. (a) Collection and Reduction of the X-ray Data. The crystals were centered on a Bruker SMART APEX II diffractometer, equipped with an APEX II 4K CCD area detector and a three-axis goniometer, controlled by the APEX2 Graphical User Interface (GUI) software,[56] and a sealed source emitting graphite-monochromated Mo Kα radiation (λ = 0.71073 Å). The diffraction data collection (at −173 °C) consisted of a full φ rotation at a fixed $\chi = 54.74°$ with 0.36° (1010) frames, followed by a series of short (250 frames) ω scans at various φ settings to fill the gaps. The crystal-to-detector distance was 4.953 cm, and the data collection was carried out in a 512 × 512 pixel mode using 2 × 2 pixel binning. Processing of the raw data was completed by using the APEX2 GUI software,[56] which applied Lorentz and polarization corrections to three-dimensionally integrated diffraction spots. The program SADABS[57] was used for the scaling of diffraction data, the application of a decay correction, and an empirical absorption correction based on redundant reflections.

(b) Solution and Refinement of the Structure. The XPREP program was used to confirm the unit cell dimensions and the crystal lattice. The final refinement was obtained by introducing anisotropic parameters for all of the atoms, an extinction parameter, and the recommended weight factor. The maximum electron densities in the final difference Fourier maps were located around the heavy atoms. All calculations were performed with the SHELXTL package for structure determination, refinement, and molecular graphics.[58] Solutions were obtained by direct methods which located the Xe and As atoms. Successive difference Fourier syntheses revealed the positions of the fluorine, nitrogen, and sulfur atoms.

Raman Spectroscopy. The low-temperature (−160 °C) Raman spectra of $[F_4S{=}N{-}Xe{---}N{\equiv}SF_3][AsF_6]$, $[F_3S(N{\equiv}SF_3)_2][AsF_6]$, and $[SE_3][AsF_6]$ were recorded on a Bruker RFS 100 FT Raman spectrometer using 1064-nm excitation and a resolution of 1 cm^{-1}, as previously described.[59] The spectra were recorded using a laser power of 300 mW and a total of 1600, 1500, and 1500 scans, respectively.

Nuclear Magnetic Resonance Spectroscopy. (a) NMR Sample Preparation. Samples containing $[F_3S(N{\equiv}SF_3)_2][AsF_6]$ and *cis*-N_2F_2 were prepared in 4-mm o.d. FEP tubes fused to lengths of ¼-in. o.d. FEP tubing fitted with Kel-F valves which contained $[F_3S{\equiv}NXeF][AsF_6]$ (ca. 0.048 g) that had been prepared in situ as previously described.[19] The samples were warmed to, and maintained at, 0 °C for ca. 20 h in $N{\equiv}SF_3$ solvent to allow the reaction of $F_4S{=}NXe^+$ with $N{\equiv}SF_3$ (eq 2) to take place. The NMR sample tubes were heat-sealed under dynamic vacuum and stored at −196 °C until NMR spectra could be obtained. Samples were redissolved at −5 °C and warmed to 0 °C just prior to data acquisition and remained at this temperature while their spectra were recorded. Low-temperature spectra were obtained from sealed 4-mm o.d. FEP sample tubes that had been inserted into 5-mm o.d. thin-wall precision glass NMR tubes (Wilmad).

(b) NMR Instrumentation and Spectral Acquisitions. Fluorine-19 NMR spectra were recorded unlocked (field drift < 0.1 Hz h^{-1}) on a Bruker DRX-500 spectrometer equipped with an 11.744-T cryomagnet. The NMR probe was cooled using a nitrogen flow and variable-temperature controller (BV-T 3000).

Fluorine-19 NMR spectra were acquired using a 5-mm combination $^1H/^{19}F$ probe operating at 470.592 MHz. The spectra were recorded in 32K memories, with spectral width settings of 24 kHz and acquisition times of 1.39 s, and were zero-filled to 64K, yielding data point resolutions of 0.36 Hz/data point. Relaxation delays of 0.10 s were applied, and 1600 transients were accumulated.

The pulse width, corresponding to a bulk magnetization tip angle of approximately 90°, was 8.5 μs. A line broadening of 0.10 Hz was used in the exponential multiplication of the free induction decay prior to Fourier transformation.

(54) Lehmann, J. F.; Dixon, D. A.; Schrobilgen, G. J. *Inorg. Chem.* **2001**, *40*, 3002–3017.
(55) Gerken, M.; Dixon, D. A.; Schrobilgen, G. J. *Inorg. Chem.* **2000**, *39*, 4244–4255.
(56) *APEX2*, release 2.0−2; Bruker AXS Inc.: Madison, WI, 2005.
(57) Sheldrick, G. M. *SADABS (Siemens Area Detector Absorption Corrections)*, version 2.10; Siemens Analytical X-ray Instruments, Inc.: Madison, WI, 2004.
(58) Sheldrick, G. M. *SHELXTL-Plus*, release 6.14; Siemens Analytical X-ray Instruments, Inc.: Madison, WI, 2000−2003.
(59) Casteel, W. J., Jr; Kolb, P.; LeBlond, N.; Mercier, H. P. A.; Schrobilgen, G. J. *Inorg. Chem.* **1996**, *35*, 929–942.

The ^{19}F spectra were referenced externally at 30 °C to a sample of neat $CFCl_3$. The chemical shift convention used is that a positive (negative) sign indicates a chemical shift to a high (low) frequency of the reference compound.

Computational Methods. Quantum-chemical calculations were carried out using B3LYP, PBE1PBE, and MP2 methods as implemented in the Gaussian 03 program[60] for geometry optimizations and vibrational frequencies and intensities for the $F_4S{=}N{-}Xe{---}N{\equiv}SF_3^+$ adduct cation and the $[F_4S{=}N{-}Xe{---}N{\equiv}SF_3][AsF_6]$ and $[F_3S(N{\equiv}SF_3)_2][AsF_6]$ ion pairs. The aug-cc-pVTZ[61] basis sets, as implemented in the Gaussian program, were utilized for all elements except Xe and As, for which the semirelativistic small core pseudopotential basis sets, aug-cc-pVTZ-PP, were used. The combined use of aug-cc-pVTZ and aug-cc-pVTZ-PP basis sets is indicated as aug-cc-pVTZ(-PP). The program GaussView[62] was used to visualize the vibrational displacements that form the basis of the vibrational mode descriptions given in Tables 4 and 5.

Acknowledgment. The work described in this paper is dedicated to the memory of our colleague and good friend, Professor Neil Bartlett (September 15, 1932 to August 5, 2008), the discoverer of noble-gas reactivity. We thank the Natural Sciences and Engineering Research Council (NSERC) of Canada for financial support in the form of a Discovery Grant (G.J.S.), the Ontario Ministry of Training, Colleges and Universities and McMaster University for the award of graduate scholarships (G.L.S.), and SHARCNet (Shared Hierarchical Academic Research Computing Network; www.sharcnet.ca) for computational resources. We also thank Dr. H. P. A. Mercier for assistance with computations, and for insightful discussions.

Supporting Information Available: Experimental Raman frequencies and intensities for $[SF_3][AsF_6]$ (Table S1); correlation diagrams and selection rules for the vibrational modes of $[F_4S{=}N{-}Xe{---}N{\equiv}SF_3][AsF_6]$ (Table S2) and their discussion; correlation diagram and selection rules for the vibrational modes of the $[F_3S(N{\equiv}SF_3)_2][AsF_6]$ ion pair (Table S3) and its discussion; NBO charges, valencies, and bond orders for $F_4S{=}NXe^+$ and $F_4S{=}N{-}Xe{---}N{\equiv}SF_3^+$ (Table S4); NBO charges, valencies, and bond orders for $F_3S{\equiv}NXeF^+$ and $N{\equiv}SF_3$ (Table S5); NBO charges, valencies, and bond orders for $[F_3S(N{\equiv}SF_3)_2][AsF_6]$ (Table S6); the Raman spectrum of $[SF_3][AsF_6]$ (Figure S1); complete reference 60; and X-ray crystallographic files in CIF format for the structure determinations of $[F_4S{=}N{-}Xe{---}N{\equiv}SF_3][AsF_6]$ and $[F_3S(N{\equiv}SF_3)_2][AsF_6]$. This material is available free of charge via the Internet at http://pubs.acs.org.

(60) Frisch, M. J.; et al. *Gaussian 03*, revision B.04; Gaussian, Inc.: Pittsburgh, PA, 2003.
(61) Dunning, T. H., Jr. *J. Chem. Phys.* **1989**, *90*, 1007–1023.
(62) *GaussView*, release 3.0; Gaussian Inc.: Pittsburgh, PA, 2003.